Erosion Mechanisms below a vertical plain Jet on a Non-Cohesive Soil Bed

by

Chi-Fung Wu

to obtain the degree of Master of Science
at the Delft University of Technology,
to be defended publicly on August 7, 2018 at 2:00 PM.

Student number:	1373749	
Thesis committee:	Prof. dr. ir. C. van Rhee	TU Delft
	Dr. ir. G.H. Keetels	TU Delft
	Dr. ir. M. van Damme	TU Delft

This thesis is confidential and cannot be made public until December 31, 2019.

Delft University of Technology

Abstract

This experimental research is focused on fail mechanisms in non-cohesive soil beneath the jet with a Jet Erosion Test(JET). A vertical plain jet impinges fluid to a sand bed, which causes zero shear stress beneath the jet averaged over time. Many erosion theories would say that no pick-up happen at that point.

$E_c = \frac{u}{\sqrt{H/d}\sqrt{\Delta g D_{50}}}$

Large range of erosion parameter was done in this research with video recordings to the activities beneath the jet. Tests varies with those parameters outflow velocities, stand off distances(SOD) and grain sizes. Comparisons are made to Rajaratnam, who has executed similar JET with varies erosion parameter too. The cavity depths and hill heights correspond well as function of the erosion parameter. Cavity widths have deviations for values above 4.0, which might cause by different grain properties or by the limitation of flume width. Secondary flow limits the width growth over time.

Weak deflected jet showed only surface erosion by micro turbulence at the soil bed till erosion parameter 1.0. One smooth bed was formed between two hill tops. Static bed did not exceed the concerning sand during and after start. Increasing further the erosion parameter (1.0-5.0), soil deformation was also seen with ejection beneath the jet. Bearing capacity by Prandtl's theory was insufficient and failed the soil bed. Consequence, the inner cavity exceeds the internal friction angle of sand with dynamic erosion. Erosion parameter larger than 5.0 had a wider cavity. Grains in soil translate and rotate in the start phase by insufficient bearing capacity. Vortices sweep around the jet with chaotic particle transport in the inner cavity.

Theories of Van Rijn, Meyer Peter Müller and Van Rhee are not suitable for JET. The pick-ups rates are underpredicted in all cases, which are based on shear stress. The impinging jet has different flow field and failure mechanism, which can be better related to the jet momentum.

Acknowledgements

This report contains Chi-Fung Wu's master thesis, which is part of the master Civil Engineering at Delft University of Technology. The experiments and documentation were done in collaboration with Dredging Engineering at the faculty 3ME of the same institute.

I am grateful to the members of my committee Prof.dr.ir C. van Rhee, dr.ir. G.H. Keetels and dr.ir. M. van Damme. Their expertise and insight contributed significantly to this thesis.

I am thankful to Andrew for keeping me accompany at the laboratory during the experiments. I would also like to thank mr. Yang for lots of editing tips and Annie Wong for the English check.

Also, my gratitudes go to my parents, relatives and friends for their support during my education in Delft.

Chi-Fung (Charles) Wu

Contents

List of Figures

List of Tables

List of Symbols

Symbol	definition	unit
A	Area	m^2
c_b	Concentration above bed	kg/m^3
C_d	Drag coefficient	$-$
C_f	Friction coefficient	$-$
C_l	Lift coefficient	$-$
C_u	Uniformity coefficient	$-$
D_{50}	Median of grain size	m
d	Diameter of the nozzle	m
E	Pick up	kg/sm^3
E_c	Erosion parameter	$-$
f	Friction coefficient	$-$
Fr	Froude number	$-$
g	Gravitational acceleration	m/s^2
H	Manometric head	m
h	Placing height	m
i	Hydraulic gradient	$-$
k	Permeability	m/s
L	Length	m
m	Mass	kg
n	Porosity	$-$
p	Pressure	N/m^2
$\tilde{p}$	Mean pressure	N/m^2
p'	Pressure by turbulence	N/m^2
Q	Discharge	m^3/s
R	Perimeter	m
Re	Reynolds number	$-$
s	Impinging distance	m
S	Source	kg/sm^2

t	Time	s
T	Transport	$-$
u_0	Outflow velocity at the nozzle	m/s
$\tilde{u}$	Vertical averaged water velocity over time	m/s
u'	Vertical water velocity by turbulence	m/s
V_s	Volume solids	m^3
V_t	Volume total	m^3
V_v	Volume voids	m^3
$\tilde{v}$	Horizontal averaged water velocity over time	m/s
v'	Horizontal water velocity by turbulence	m/s
v_e	Erosion rate	m/s
v_g	Permeability at upper layer	m/s
W	Width	m
w_s	Fall velocity	m/s
x	Cavity width (distance top to top)	m
α_{rec}	Entrainment coefficient	$-$
β	Bed slope angle	$^\circ$
ϵ	Cavity depth	m
Δ	Specific gravity	$-$
$\Delta\epsilon$	Hill height	m
θ	Shields parameter	$-$
μ	Kinematic viscosity	m^2/s
ν	Dynamic viscosity	kg/ms
ρ	Density	kg/m^3
ρ_i	Insitu density	kg/m^3
ρ_s	Density solid sand	kg/m^3
ρ_w	Density water	kg/m^3
$\tilde{\tau}$	Averaged shear stress over time	N/m^2
τ'	Shear stress by turbulence	N/m^2
τ_b	Bed shear stress	N/m^2
τ_c	Critical shear stress	N/m^2
ϕ	Internal friction	$^\circ$
%	Percentage	$-$
$^\circ$	Degree	$^\circ$
$^\circ$C	Degree temperature	$^\circ$

Chapter 1

Introduction

As the population keeps growing and cities are becoming more populated, we see an increase in the number of people who move to the coastal areas for living, work and leisure. Investing and researching in good coastal infrastructures are therefore important. Cables and pipelines are vital components in this infrastructure. One of the cost efficient methods is the application of a moving jet for the construction method. Many studies have used with Jet Erosion Tests (JETs) to gain a better understanding of the processes that are going on beneath the nozzle. These studies give insights in how the removal of the sand bed makes it possible to build infrastructures more efficiently.

Pipelines can either be build on or in the bed to connect both sides of the sea. Salt, vessels and organisms can harm the infrastructure in the sea during its lifetime. To prolong the lifetime of the infrastructure, local conditions are taken into account when building the infrastructure. A dredging vessel can have a remote high-pressure water jet, which displaces the grains elsewhere via bed or suspension load transport. Cables are put in the excavated bed, then the cavity is covered back with soil to protect the infrastructure against the hostile environment.

Erosion theories are mainly based on shear stresses above soil bed. A lot is known about jet outflow and soil, but little is known about processes around stagnation point. Shear stresses refer to the forces on the sand particles by parallel flow in waterways. Beneath the vertical jet has no shear stresses with zero flow velocity in ideal impinging condition, because all kinetic energy will be converted to pressure at a certain distance from the impinging jet. This would mean that no pick-up would occur in the bed at the stagnation point. In practice sediment transport does occur in the alluvial bed. Hence, this study focuses on the processes that erode the sand bed at the stagnation point.

1.1 Objective

This master thesis describes the physical processes around the stagnation point with a Jet Erosion Test (JET) in various test settings. Different water flow velocity, height/diameter ratio, diameter particles, soil bed density and permeability are analysed at the dredging laboratory in Delft University of Technology at the faculty Mechanical, Maritime and Materials Engineering (3ME). This leads to the following subquestions to achieve the main objective of this research.

- What is known in the literature?
- What happens at the stagnation point in jet erosion test?
- How does the cavity develop over time using a stationary plain jet in several sand bed conditions?
- What are the sand bed failure mechanisms under different test settings?

1.2 Outline of thesis

This report proceeds as follows.

Part one is the literature study, where various JET processes and models are described. Findings about grain forces and sediment transport are also included.

Part two describes the research method. The test plan is outlined for the JET along with the various parameters. Considerations for the equipments were dependent on the limits of the flume.

In part three, the analysis is presented. This includes a description of the experiment preparation and how the equipment was used and validated in the laboratory. In addition, the experiment was run and analysed. Some test runs are discussed in this part too.

The final part consists of the conclusion and recommendations.

Chapter 2

Literature review of flow processes

In this chapter, several flow processes are described that have emerged after long vertical submerged impinging water jet. Starting with two extreme cases are the free jet and impinging jet, where the first mentioned has no blockage and the latter has a full impervious plate beneath the jet.

2.1 Velocity profiles

2.1.1 Behaviour of free jet

In the free jet condition, water flow exits unhindered from the nozzle. A mixing layer is then formed because of velocity differences in the viscous fluid after leaving the nozzle. Surrounded fluid is carried along with the jet, this is called entrainment.

The vertical jet outflow (u_0) exercises in the full width and length from the smooth contraction nozzle. The mixing layer becomes larger in width along streamwise direction from the turbulent jet, while the original vertical velocity becomes smaller in propagating direction according to Rajaratnam [1976]. This wedge-shape region is called the potential core with the vertical velocity u_0 in undeveloped regime. The length of the region is called stand of distance (SOD). This term can made dimensionless stand of distance H/d by original impinging distance divided to the nozzle width. Distances larger than the potential core are called fully developed flow regime, where only a mixing layer is present. The velocity difference induces turbulence over a small distance in viscous water.

Affected area to the soil layer becomes larger further in the propagating direction. The jet momentum spreads over a larger horizontal area. The momentum per unit of area decreases along the propagating jet distances for free jet.

2.1.2 Processes around impinging flow

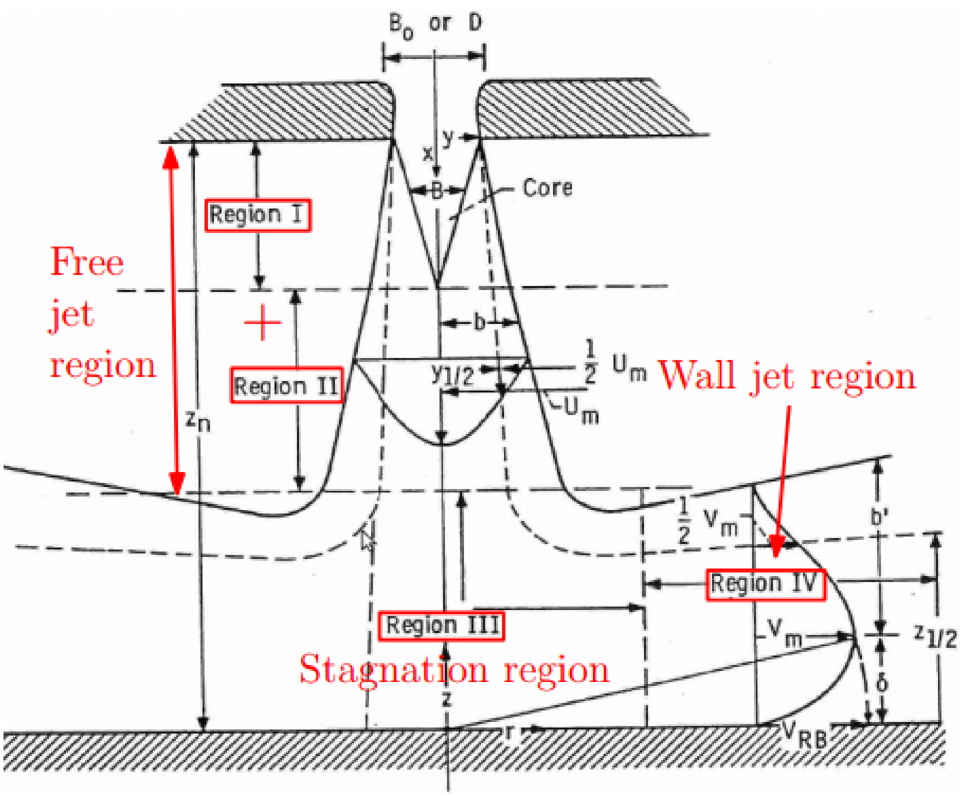

Figure 2.1: Impinging jet (Gauntner et al. [1970])

An impinging flow deflectes from a vertical to horizontal direction as it hits the impermeable wall. Vertical fluid propagates unhindered perpendicular towards the horizontal impermeable wall. Fluid bends into parallel directions to the wall with conservation of volume. Vertical kinematic energy converts to pressure head as it reaches the bottom as can be explained through Bernouilli equation 2.1. The pressure difference with the ambient water bends the flow in lateral directions. In addiction, the volume balance forces the incompressible water from incoming vertical to sideways directions. A perfect impinging jet is shown without entrainment in Figure 2.1.

$$z + \frac{P}{\rho g} + \frac{u^2}{2g} \tag{2.1}$$

The energy losses is assumed to be zero for the relatively small impinging distances. Another assumption is that all kinematic head is converted to pressure head at the bed with incompressible fluid. The stagnation pressure beneath the bed can be written as:

$$P = \rho g h + \frac{1}{2}\rho u^2 \tag{2.2}$$

Wall jet is the parallel flow above the impervious wall. Velocity-in-depth profile becomes a square root form perpendicular to the wall with zero velocity (r_max) at the bed bottom. Shear stress is determined by the depth-averaged velocity between the eye and instant bed geometry. The roughness of the wall effects the velocity profiles in the water column. If shear stress exceeds the resistance, particles will erode until the bed is in equilibrium.

2.2 Flow development from turbulent jet

Water pumps vary in discharge in seconds for several reasons because of turbulence. de Vriend et al. express velocity using two terms in analytical terms to the instant actual value as in equation 2.3. The first term ($\tilde{u}$) is the mean value over time and thesecond term (u') is the instant fluctuating component. These combined are shown for flow velocity as following:

$$u = \tilde{u} + u' \tag{2.3}$$

Shear stress causes by water is defined in equation 2.4 as:

$$\tau = 0.5 c_f \rho_w u^2 \tag{2.4}$$

Shear stress is a function of the average shear velocity above the sand bed and the vortex eye, which has the shape as shown in Figure 2.2 for an impinging jet at the original bed level.

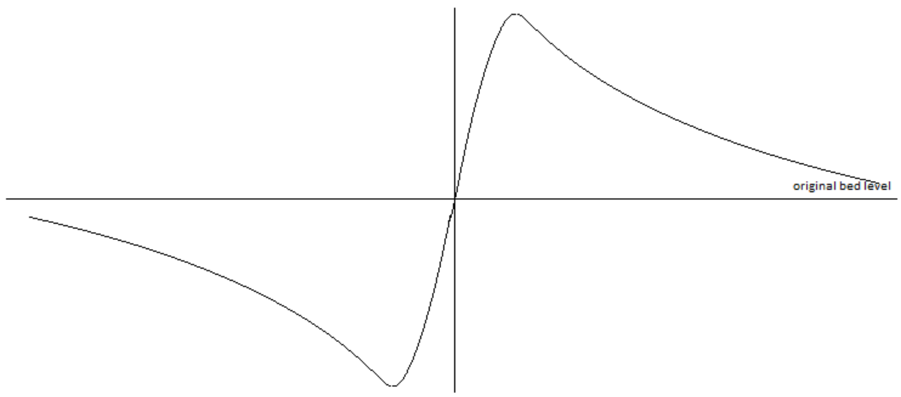

Figure 2.2: Theoretical shear stress

Entrainment increases the jet discharge along the viscous water flow. Ambient water is sucked into the propagating direction. The discharge increases in the mixing layer. The volume transport increases in the propagating flow as:

$$u_s = f_1 \sqrt{\frac{H_{nozzle}}{H_{imp}}} u_0 \tag{2.5}$$

$$\frac{\delta Q}{\delta s} = \alpha_{ent} R u_s = \alpha_{ent} 2 L f_1 u_0 \sqrt{\frac{H_{nozzle}}{H_{imp}}} \tag{2.6}$$

Alberson et al. [1950] derived the entrainment coefficient with value of $\alpha_{rec} = \frac{1}{2f_1^2} = 0.091$ for a plain impinging jet. f_1 is an empirical constant between 2.35 and 2.45 as stated by Fischer et al. [2013]

where H_{nozzle} is the nozzle diameter. s is the distance from the jet until the sand bed. R is the length of the hypotenuse.

The depth averaged velocity is retrieved as follows. The discharge grows in propagating water because of entrainment. Then, the volume splits on two sides of the plain jet, where in assumption half of the discharge flows to one side of the centreline. The half discharge is divided by the flow area between the eye of the vortex and the insitu bed geometry.

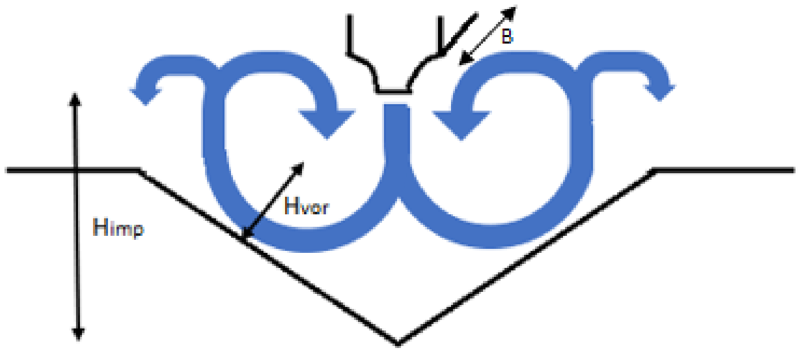

Figure 2.3: Schematic flow in the cavity

$$u_m = \frac{1}{2}\frac{Q_{imp}}{Bh_{vortex}} \tag{2.7}$$

The motion of an unit fluid can be expressed by the momentum equation Battjes [2002].

$$\frac{\partial u}{\partial t} + u\frac{\partial u}{\partial x} + v\frac{\partial u}{\partial y} + w\frac{\partial u}{\partial z} = \frac{1}{\rho}\frac{\partial P}{\partial x} + \nu(\frac{\partial^2 u}{\partial x^2} + \frac{\partial^2 u}{\partial y^2} + \frac{\partial^2 u}{\partial z^2}) \tag{2.8}$$

The first term in equation 2.8 is not relevant since the discharge is assumed to be constant without any source of fluid. The second term cannot be neglected, since the streamline changes direction from the longitudinal to the lateral directions. The third term means that the stagnation pressure is different at inconsistent impinging distances. The last term is the turbulence accounting for energy losses during the flow.

Volume balance can be described as:

$$\frac{\Delta Q}{\Delta t} + A\frac{\Delta u}{\Delta x} = 0 \tag{2.9}$$

Turbulence is present in any jet in viscous fluid. Propagating water exercises some instabilities after leaving the jet in the mixing layer because of velocity differences over short distances, which change the terms in the momentum. The stresses in non-uniform flow is influenced by the following parameters: fluid density, sediment density, kinematic viscosity, grain size and bed shear stress. These factors cause turbulence to the water stream and result into shear stress. The interaction makes the water stream and the bed as vortex slightly variable. Reynolds numbers are used to describe the quality of turbulence. The equation is the ratio of inertia force divided by the viscous force:

$$Re = \frac{inertiaforce}{viscousshearforce} = \frac{U_0 D}{\nu} \tag{2.10}$$

A method to describe the varying turbulence flow is the Reynolds Averaged Navier Stokes(RANS). The vertical outflow velocity shows some fluctuation beneath the je. Any fluctuations (2.3) are left out during test to make it easier to approximate the hydraulic turbulence.

Chapter 3

Literature review of soils

In this chapter, theories are investigated for non-cohesive soil as grain properties and pick-up. This report will mainly cover sand soil, including small section about properties of glass beads and bentonite.

3.1 Properties of non-cohesive soil

Nature is capricious as every particle is unique due to differences in diameter, shape and chemistry content. Environmental factors impact saturated rocks high in the mountain through internal tensions caused by temperature differences. Further downstream, rocks abrade in a propagating river to the size of a sand grain in the ocean. Sand is a non-cohesive soil, which means that the particles do not stick together.

Solid sand particles have void spaces in an unit of soil. Voids leads to permeability of the sand bed so that fluid can be passed through in relative low velocity, if pressure gradient is present. A saturated sand bed and a sudden large load can cause dilatations or compaction in incompressible fluid. Soil properties changes temporarily with failure consequences on the bed.

Sand is a common soil type that occurs in nature, it comes from the wearing of larger rocks from mountains upstream that ends up int he river. A particle with a diameter between $63\mu m$ and $2mm$ is classified as sand, the sand size is between that of thesilt and gravel soil type as can be seen in Table 3.1 from Verruijt and Baars [2007]. The chemical compositions comprise from siliciumdioxide and quartz. The interaction between particles depends on the dimension, shape of the particles, density, particles size distribution, chemical composition and porosity.

Type	Subclass	Diameter (mm)
Gravel	Medium gravel	8.0-16.0
Gravel	Fine gravel	4.0-8.0
Gravel	Very fine gravel	2.0-4.0
Sand	Coarse sand	0.63-2.0
Sand	Medium sand	0.2-0.63
Sand	Fine sand	0.063-0.2
Silt	Coarse silt	0.02-0.063
Silt	Medium silt	0.0063-0.02
Silt	Fine silt	0.002-0.0063

Table 3.1: Classification for gravel, sand and silt

Particle sieving analysis is a useful method to examine sand soil. Properties like the median grain diameter D_{50} can be determined from a representative sand sample. Additional analysis is possible to get the uniformity coefficient, the internal friction angle and fall velocity.
A qualitative description to a unit soil volume is porosity, which is defined as the ratio of voids volume to the total soil volume.

$$n = \frac{V_{\mathrm{v}}}{V_{\mathrm{t}}} \tag{3.1}$$

3.1.1 Properties of glass beads

Glass beads are made from the manufacture Sigmund Lindner GmbH in Germany. Beads are generally used for abrasive blasting in industrial sector. The transparent beads smooths mechanically the object surface from any dust and contamination to a clean material. The surface of object will strengthen and smoothen after blasting the material. The beads are made from silicium, which hardly reacts to other elements.

The beads are made in a controlled manufacture. The particles size distribution is generally very bad graded. Besides, the roundness would classified as spherical. Consequently, the beads result to an homogeneous bed state.

3.1.2 Properties of bentonite

Bentonite reduces interaction between the voids of sand. Permeability is reduced by the swollen bentonite with the characteristics of sand soil. Bentonite is characterized as small particles with a diameter of $0.2 - 2\mu m$. This material is considered as impermeable soil in wet state. A mixture of sand and bentonite takes time to collaborate for being a impervious soil bed. Voids are barely connected to each other, which makes permeability almost impossible.

3.2 Bearing capacity

Hypothese 3 is the soil movements by insufficient bearing capacity. The book of Verruijt and Baars [2007] describes the vertical downward pressure as Prandtl's zones. The movements are schemetised in Figure 3.1 and can be divided in three zones. The vertical hydraulic stresses are represented by the vertical and horizontal forces in zone III, displayed as a triangle shape. Excess stress in that wedge pushes the soil upwards in region I to above the original bed level. This is caused by insufficient resistance of region I. Zone II is the transition between zone I and III. Shear stress is at maximum between those zones. The bearing capacity can be determined by the theory of Prandtl. Brinch Hansen extended the formula with the factors inclination, shape, cohesion and friction angle for a two-dimensional soil bed. This theory has the following assumptions: weightless material, homogeneous bearing material, no volume change, uniform distributed loading and plastic behaviour during deformation. The acting force on the soil can be inclined. p is the vertical vector and t is the horizontal component in Figure 3.1.

Bearing capacity according to Prandtl of soil can be expressed using the following formula.

$$p = i_c s_c c N_c + i_q s_q q N_q + i_\gamma s_\gamma \frac{1}{2} \gamma B N_\gamma \tag{3.2}$$

If cohesion in the bed is equal to zero, the first term equal to zero. The second term is also equal to zero. A flat sand level has no surcharge around the bearing area, which reduces the resistance of a burst. Only, the third term is left in the equation. The vertical downward hydraulic momentum

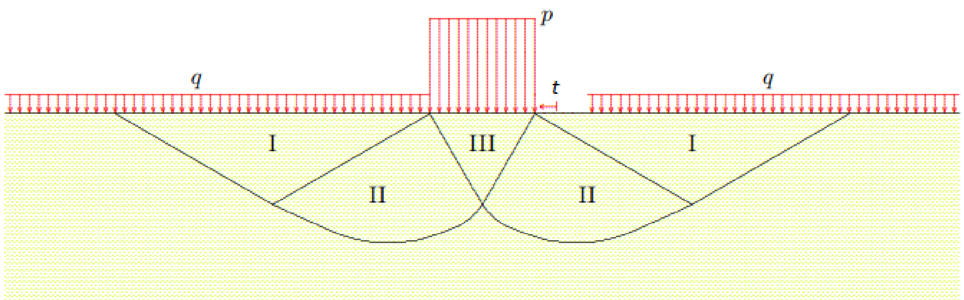

Figure 3.1: Schematization of bearing capacity (Verruijt and Baars [2007])

acts as a strip load on the sand bed, which might lead to potential soil failure.

Prandtl includes the following factors for the bearing capacity of soil:

$$N_c = (N_q - 1)\frac{1}{tan\phi} \tag{3.3}$$

$$N_q = \frac{1 + sin\phi}{1 - sin\phi}e^{\pi tan\phi} \tag{3.4}$$

$$N_\gamma = 2(N_q - 1)tan\phi \tag{3.5}$$

Shape factors $B \leq L$

$$S_c = 1 + 0.2\frac{B}{L} \tag{3.6}$$

$$S_q = 1 + \frac{B}{L}sin\phi \tag{3.7}$$

$$S_\gamma = 1 - 0.3\frac{B}{L} \tag{3.8}$$

Inclination of forces are determined with these factors:

$$i_c = 1 - \frac{t}{c + ptan\phi} \tag{3.9}$$

$$i_q = i_c^2 \tag{3.10}$$

$$i_\gamma = i_c^3 \tag{3.11}$$

Chapter 4

Literature review of erosion

4.1 Erosion mechanics

Particles are moved over distances by a driven force as individual grain or as bulk volume. Particles are picked up individually when there subject to lower propagating hydraulic forces. Individual grains are exposed to the hydraulic forces and experience resistance on the sand bed. Larger momentum leads to erosion in bulk or soil deformation. Other distinction is the erosion in vertical or horizontal direction.

Several types of force are introduced to an individual grain from reader Molenaar and Voorendt [2012] first. Then, bulk transport is described in the second part.

4.1.1 Forces on individual particles

Drag is the horizontal force acting on a grain through viscous fluid in the same direction. The force is a function of the drag coefficient, density, flow velocity and the exposed area of the grain.

$$F_D = \frac{1}{2} C_D \rho u^2 A \tag{4.1}$$

Lift is the force in thevertical upward direction caused by horizontal flow. The velocity difference and the grain shape lead to pressure gradient on a single particle between the upper and lower surface, which could lift up the particle.

$$F_L = \frac{1}{2} C_L \rho u^2 A \tag{4.2}$$

The weight of a single particle excites vertical downward force because of gravity.

$$F_g = mg = \rho V g \tag{4.3}$$

Force gradient occurs if pressure gradient is present on particles in the top layer. Dilatation or compaction can result in pressure differences between the upper and lower surface of an individual particle for a short time under those circumstances.

$$F_1 = F_0 + \Delta F \tag{4.4}$$

Vertical incipient motion starts when the combination of driven forces is larger than the resistance forces on a single particle. The following equation defines incipient motion.

$$F_D + F_L < F_g \tag{4.5}$$

Soil erodes particles at the micro level, when loading forces is just larger than the resistance. The pick-up rate is very small in general. The transport modus of scoured particles is bed load or suspended load for short distances.

Very loose soil beds have a relatively large void space per unit of volume. Solid particles can settle in the little voids because of compaction with external hydraulic force beneath the jet. If the sand soil is packed, particles settle less likely by leak of void space. Solid grains have no space to pack the soil bed, instead it will pick-up or push as active soil beneath the jet.

Since every grain has a different position, the characteristics for individual particle differ too in terms of:

- Position compared to other particles
- Weight of a single particle
- Exposed area of grain in fluid
- Chemical content of a particle

4.1.2 Processes around bulk erosion

This section describes the pick-up rate of bulk volume from a larger jet momentum. A layer of sand are transported closed to the bed in a high concentration.

Bisschop [2018] distinguishes two regime in horizontal erosion, namely saltation and bulk erosion. Saltation entrained a few grains on the soil surface into the flow. This process happens with the Shields parameter just above the critical value. Bulk erosion moves the toplayer of grains as a bed load in horizontal directions. The grains are displaced at large Shields parameter.

Pick-up can be calculated by dividing the eroded bed volume by the bed density. The pace in height is called the erosion velocity. The insitu soil is a mixture of solids and void. Pick-up rate is calculated by dividing density.

$$v_e = \frac{E}{\rho_s(1 - n_0)} \tag{4.6}$$

4.1.3 Pick-up of sand

Shields parameter is used to calculate the incipient motion of grains on a flat bed with parallel flow. The nondimensional parameter is an empirical function of the shear force and the submerged weight of a single particle. Pick-up takes place, when the critical Shields parameter exceeds the threshold value according to the book by Schiereck [2003]:

$$\theta = \frac{\tau_b}{(\rho_s - \rho_w)gD_{50}} \tag{4.7}$$

Rajaratnam [1981] adapted the Shields parameter and translated it to an erosion parameter by adding the initial impinging distance SOD-term, then dividing it by the square root. Rajaratnam defined the erosion parameter for plain jet as:

$$E_c = \frac{U}{\sqrt{H/d}\sqrt{\Delta g D_{50}}} \tag{4.8}$$

The erosion parameter is a good indicator for the final cavity dimension of a JET. A linear correlation has been made for the erosion parameter as function of dimensionless cavity depth, width or hill height.

The bed state can be distinguished in two geometries: weak deflected jet and strong deflected jet. The first mentioned has a smooth cavity shape from hill to hill. The deflected jet is attached to the bed along the entire erosion zone. The grains are transported radially outward as bedload. The strong deflected jet has bed deformation inside the outer region. The inner cavity has a steep slope until the flow separation.

Turbulence has flows with different velocities and directions. The instability causes turbulent behaviour such as ejections and sweeps at the sand bottom Nezu et al. [1993]. Ejection is characterised by a local vertical and horizontal velocity lower than the depth-averaged flow velocity. Sweep has a larger local horizontal velocity than the depth-averaged flow velocity.

4.1.4 Sedimentation

Sedimentation settles the particles in suspended load on the sand bed. Increase in bed height can be seen as a reverse of erosion. Causation is generally the leak of a driven force to the particle, which settles by gravity. High sand concentration hinders temporarily settlement of suspended grains, which increases the sedimentation time. Fluid can not escape through the voids with the decreasing space.

This thesis mainly focuses on erosion. Any sedimentation during the tests were not included in the pick-up and transport rate. A simple sediment equation is stated as:

$$S = c_b w_s \tag{4.9}$$

Settling velocity is defined as:

$$w_{\mathrm{s}} = \sqrt{\frac{4g\Delta D_{50}}{3C_d}} \tag{4.10}$$

4.2 Theories about sediment transport

Well-known erosion theories base particle transport on the horizontal stress load, see for example the theories by Van Rijn, Meyer-Peter Müller and Van Rhee. Empirical experiments are mainly based on shear stress and particle properties at the bed. Particle transport with an increasing or decreasing bed height could be regarded as pick-up in vertical direction.

4.2.1 Van Rijn

Many experiments were done with pick-ups of single particles in the range between 0.13 and $1.5mm$, according to Rijn [1984]. Those tests were with shear flow velocity up to $1m/s$. Particles start when hydraulic force exceeds the resistance on a grain. The empirical transport and dimensionless diameter is defined as:

$$T = \frac{\tau_b - \tau_{b,cr}}{\tau_{b,cr}} \tag{4.11}$$

The transport function could also be written as:

$$T = \frac{\theta - \theta_{cr}}{\theta_{cr}} \tag{4.12}$$

Dimensionless particle diameter is defined as a function of:

$$D_* = D_{50}(\frac{\Delta g}{v^2})^{1/3} \tag{4.13}$$

Combining equations 4.11 and 4.13 result in the empirical pick-up rate:

$$E = 0.00033\rho_s\sqrt{\Delta g D_{50}}D_*^{0.3}T^{1.5} \tag{4.14}$$

This function is described as the mass of eroding soil per unit of area and time Rhee [2015]. This equation is a good approximation for the pick-up rate caused by the hydraulic shear flow above the sand bed.

The erosion velocity scoured in depth, is the distance per unit of time. The pick-up is divided by the insitu bed density to get the erosion velocity in bed, which is defined as:

$$V_e = \frac{E - S}{\rho_s(1 - n)} \tag{4.15}$$

4.2.2 Meyer-Peter and Müller

Experiments with sand bed-load transport have been conducted with particles larger than $0.4mm$. This theory defines the incipient motion differently from the previous model. The mobility parameter is as follows de Vriend et al.:

$$\Phi = 8(\theta - \theta_c)^{1.5} \tag{4.16}$$

With dimensionless mobility number, bed load transport can be determined with:

$$\Phi = \frac{E}{\sqrt{(\frac{\rho_s - \rho_w}{\rho_w})gD_{50}^3}} \tag{4.17}$$

The pick-up function is then:

$$E = 8(\theta - \theta_c)^{1.5}\sqrt{(\frac{\rho_s - \rho_w}{\rho_w})gD_{50}^3} \tag{4.18}$$

The main difference is the dimensionless transport parameter compared to the theory by Van Rijn. The first part of the term is to the power of 1.5, but without dividing to θ_{cr}. Critical theta is smaller than the value one, which lowers the pick-up rate on the one hand, but multiplies with factor 8 on the other hand.

4.2.3 Van Rhee

This theory deals better with the high velocity shear flow as a consequence of pore volume increase in a short time (Rhee [2015]). The theory extends the theory of Van Rijn with a correction for high flow. A sudden shear movement in the sand bed would trigger temporal dilatation. Pore pressure decreases suddenly in the soil layer, which results in hydraulic gradient on the bed. Incompressible fluid cannot fill up the increased pore volume due to low permeability. Water pressure hinders erosion in the bed for a short time.

Another relevant mechanism is the stability of a particle on a slope. The actual maximum slope angle β could be larger than the internal friction angle ϕ, if an external force is present against active sliding soil. Shear stress caused by water leads to drag force F_s and hydraulic gradient F_i in soil, which takes into account the high water shear flow. The submerged weight of sediment is defined as F_g. The forces are shown on a single particle at a slope:

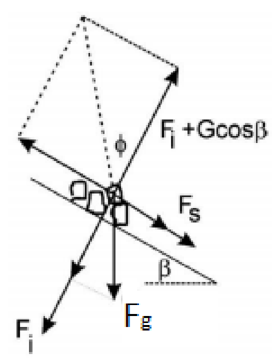

Figure 4.1: Forces on particle at slope

The force of a single particle is critical, when the internal friction force is fully used. Incipient motion of a single particle starts, when the angle between the normal force and resulting force exceed ϕ angle. Critical force balance is defined as:

$$F_s + F_g sin\beta = (F_g cos\beta + F_i) tan\phi \tag{4.19}$$

Rhee and Bezuijen [1992] approaches the stability with two different methods: Single particle and Continuum.
Single particle

$$F_g = {}^1\!/_6 \pi {D_{50}}^3 (\rho_s - \rho_w) g \tag{4.20}$$

$$F_i = {}^1\!/_8 \pi {D_{50}}^3 \rho_w g i \tag{4.21}$$

Continuum

$$F_g = (1 - n_0)(\rho_s - \rho_w) g \tag{4.22}$$

$$F_i = \rho_i g i \tag{4.23}$$

Incipient motion starts on a flat surface, if actual Shields parameter exceeds the adapted critical parameter:

$$\theta > \theta_{cr,rhee} \tag{4.24}$$

Pick-up rate E is almost the same as Van Rijn with an adapted Shield parameter, but including permeability. Erosion rate can be defined as:

$$v_e = \frac{E - S}{\rho_s (1 - n_0 - c_b)} \tag{4.25}$$

$$\theta_{cr,rhee} = \theta_{cr} \left(\frac{sin(\phi - \beta)}{sin\phi} + \frac{v_e}{k} \frac{n_i - n_0}{1 - n_i} \frac{A}{\Delta} \right) \tag{4.26}$$

$$E = \phi \sqrt{g \Delta D_{50}} \tag{4.27}$$

$$\phi = 0.00033 D_*^{0.3} T^{1.5} \tag{4.28}$$

$$E = 0.00033 D_*^{0.3} \left(\frac{\theta - \theta_{cr,Rhee}}{\theta_{cr,Rhee}} \right)^{1.5} \sqrt{\Delta g D_{50}} \tag{4.29}$$

Van Rhee includes permeability in the adapted Shields parameter, which is important at high flow velocity. The pick-up rate decreases due to permeability term in equation 4.26. A gradient in top soil layer is defined as:

$$i = \frac{v_g}{k} \frac{n_i - n_0}{1 - n_i} \tag{4.30}$$

Chapter 5

Set-up of the experiment

The design and the set-up of the jet erosion test are described in this chapter. The first section shows the required equipments of the experiments. The execution is described in the second section for several test series. The main experiments took place in the acrylic flume at the Dredging laboratory of faculty Mechanical, Maritime and Materials Engineering in Delft University of Technology.

5.1 Experimental set-up

All experiments were executed in the front compartment in the fully width of the flume. An extra divider with a height of $0.7m$ was built to reduce lateral flow around the jet. The water level was in all compartments at $0.9m$. Figure 5.1 shows the schematic side view of the experiment including the water system. The flume is located in a controlled environment with a temperature around $20°C$, the water temperature was also around $20°C$. The directions are defined as xyz-directions. X is longitudinal, y is lateral and z is normal direction.

These following items were used to execute the experiment:

- Pump
- Splitter $G1\frac{1}{4}$
- Water discharge meter (Flowtec Variomag)
- Valves $G1\frac{1}{4}$
- Tube $G1\frac{1}{4}$
- Jet
- Hose

- Impinging table
- Pressure gauges; Rosemount 1151 Smart
- Sand
  - Dorsilit 5F
  - Dorsilit 7
  - Dorsilit 8
- Glass beads
  - Small
  - large
- Camera
  - GoPro Silver Hero 3+
  - Fastcam APX RS Photron

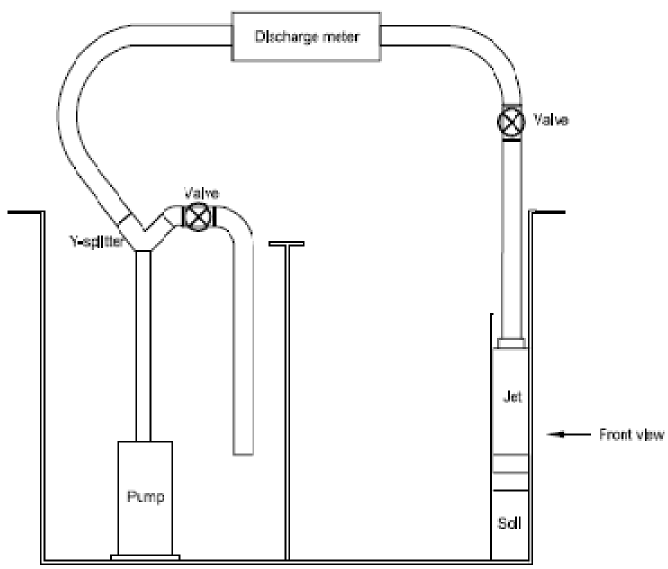

Figure 5.1: Side view of test setting

The flume has the dimensions $1.5x0.75x1.0mm$ (LxWxH) with a $0.7m$ divider in the front compartment. The walls and the divider are made from transparent acrylic of $10mm$ thickness. A frame holds the stainless tube and the jet in place. The nozzle has a two-quarter funnel shape with a $2.5mm$

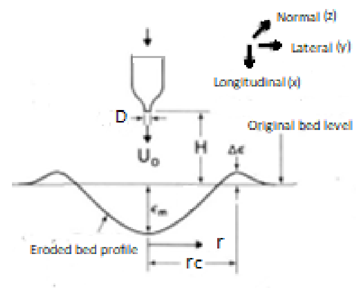

Figure 5.2: Directions

outflow width. The length of the jet is a compromise between minimise sediment placements on the drag head and the hydraulic interaction on both side of the jet. Valves can be adjusted beforehand for the right outflow velocity, a constant momentum from the nozzle. Jet height could be adjusted to meet the test requirements via two bolts in the rigid overhanging frame. Technical drawings for jet and the frame can be seen in B along with more details about the set-up. Soil is filled to $0.2m$ height in all test cases and spread evenly over a homogeneous bed.

Two pressure gauges (Rosemount) measured in the range between 0.0 to $7.0kPa$ beneath the jet for the flow characteristics. The computer can show instantly the vertical local pressure beneath the jet. Two hoses are connected with the gauges for validating the absent of lateral flow at $0.2m$ height. The first gauge is located right beneath the nozzle at the same level as the bed at the half length of the plain jet ($50mm$) from the front wall. The second gauge is placed beneath the jet, $15mm$ behind the front wall. Before executing the experiment, gauge hoses are filled with fluid, to make sure that no air is trapped in the measuring system for reliable results.

5.2 Execution of experiments

This research examines what happens for different variables inside the erosion parameter. The variables are outflow velocity, stand off distance (abbreviation SOD), grain size and density of soil. Each run has to be checked first on the following points: valves, frame, water jet, the sand bed and the camera. After going through the checklist, the test could be executed until the cavity has reached the dynamic equilibrium.

The first series of tests were performed with a fully impermeable impinging jet and free jet, which differ in flow characteristics. Two gauges were mounted to measure the pressure beneath the jet. Before the tests were run, outflow velocity, SOD and equipments were checked. Extra attention was paid whether the gauges were placed correctly beneath the pain jet at $15mm$ and $50mm$ behind the front wall.

The second set of experiments was conducted with various velocities on permeable loose sand bed. The flat homogeneous sand bed was carefully prepared for each run. The sand mass was measured before each run to know the density of the bed. The soil bed was made homogeneous and flat before every run. One test setting were executed three times for more reliable comparisons. The valve on the jet was essential to control for the outflow velocity.

The third series of tests was executed with different SODs. The impinging height could be adjusted via the two bolts on the overhanging rigid frame.

The fourth tests sequence were tests with three different particle diameters, namely D_{50} 0.63, 0.93 and $1.41mm$. The sand volumes were then further analysed for more detailed information. This analysis can be found in appendix A. The front compartment was cleaned every time after changing for a different sand bed.

The fifth set was tested on dens soil bed. The loose soil state was tested first before a dens test was executed. A long vibrator was used to pack the soil bed. Extra grains were added in the specified soil volume, which leads to a denser state. After all the preparations, it was assumed that there was a homogeneous dens bed of the soil.

The sixth series were executed with perfect spherical glass beads under several conditions. Beads were sieved in StevinLab II at the faculty Civil Engineering in order to measure the diameter and distributions. More information about this can be found in Appendix A. A black curtain was used in the background to brighten it up and increase contrast from the beads.

The last series was executed with bentonite. Bentonite was added with a 6.0% volume percentage to the non-cohesive sand soil, which is equal to 3.6% mass percent of sand weight. Permeability decreases significantly with this bed mixture, according to Foortse [2016]. The well mixed sand and bentonite was measured in dry state and put in the front compartment. Water was carefully added, so that the bentonite would not move through the voids. This set-up had to rest at least 24 hours to reduce the permeability in sand.

5.3 Determination of results from experiments

Important aspect is the pick-up rate as function of shear stress. Calculation for the shear stress is described in this section. The mean discharge from the jet is measured with the electromagnetic flow meter. The discharge will increase in the distance between the nozzle and the sand bed by entrainment. (see eq. 2.5) The discharge at the bed is assumed to split half to one side, the other half to another side. The mean shear velocity is determined as followed, the half discharge is divided by the flow area between the eye of the vortex and the insitu bed geometry (see eq. 2.7). A schematic flow pattern can be seen in Figure 2.3. The bed shear stress is, then, calculated with equation 2.4 with a constant $c_f = 0.004$.

$$u_s = f_1 \sqrt{\frac{H_{nozzle}}{H_{imp}}} u_0 \tag{5.1}$$

$$Q_s = \alpha_{ent} 2 s u_s \tag{5.2}$$

$$u_m = \frac{1}{2} \frac{Q_s}{B H_{vor}} \tag{5.3}$$

$$\tau = 0.5 c_f \rho_w u_m^2 \tag{5.4}$$

This research deals only with pick-up without any sedimentation. The scoured cavity is in the form as two triangle. The pick-up rate is the width times the depth for a consecutive time step. This method is done till recirculated suspended grains start settling in the cavity. Sedimentation can, therefore, set to the value zero. Then, the pick-up rate is calculated by rewriting equation 4.6, which will be analysed in the next chapter.

$$E = v_e \rho_s (1 - n) \tag{5.5}$$

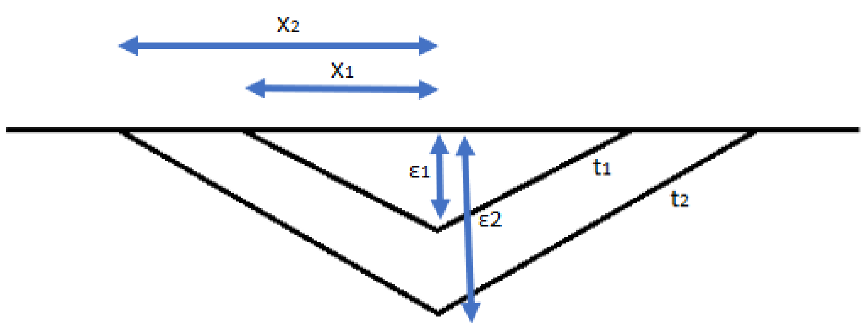

Figure 5.3: Model for pick-up rate

Chapter 6

Hypotheses

I expect particle movements beneath the jet by because of one of the following reasons:

1. Small hill inside the cavity will be formed, pick-up occurs only in presence of shear stress. The shear stress entrained the particles up to form a cavity around the centerline as in Figure 6.1. Zero shear stress averaged over time would not pick-up any particles.

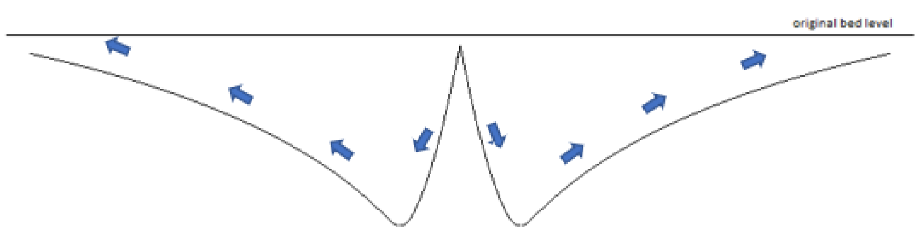

Figure 6.1: Cavity with hill

2. Pick-up is caused by shear stress on the bed surface. A smooth cavity is formed in the soil as in Figure 6.2. Turbulence part of velocity erodes the hill beneath the jet.

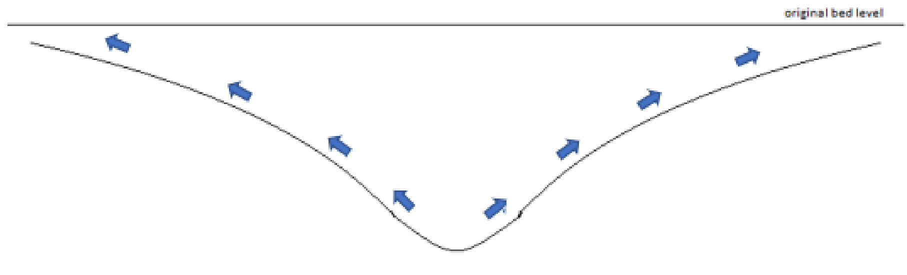

Figure 6.2: Weak deflected jet

3. Vertical flow pushes the soil bed and dragged the particles as ejection away. Sediments going downwards would be observed beneath the jet as Prandtl. Surrounded soil can not resist the bed deformation. Fluid follows the cavity geometry. The eroded particle are dragged along the bed. Dynamic bed will be as strong deflected jet.

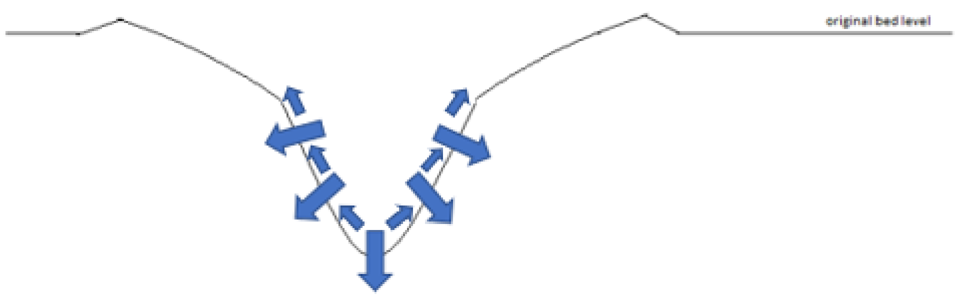

Figure 6.3: Bed deformation with ejection

4. The particles are pushed away as a ejection in combination with sweeps. Grains are deformed in the bed at the beginning of the experiment. Surrounding soil has insufficient weight to resist any bed deformation. The grain movement will translate and rotate away from the centerline. The final bed state takes as strong deflected jet.

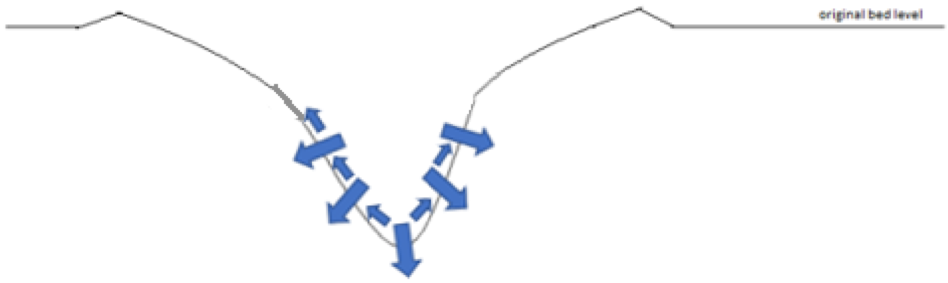

Figure 6.4: Bed deformation with sweep

Chapter 7

Analysis of experiments

This chapter is divided in three parts to answer the research objectives. The first part presents the particle sieving analysis. The grain properties are derived from Dorsilit. The second part presents the comparison with plain impinging jet from the study of Rajaratnam [1981]. The third part presents the observations from the processes for low and large erosion parameter values beneath the JETs. Videos and results were analysed in the start, asymptotic and end phase. Pick-up rates are considered for some test cases. The fourth part present the experiments with glass beads and bentonite. Pick-up processes are compared with Dorsilit sand soil.

7.1 Analysis particles

7.1.1 Sand

Dorsilit 5F, 7 and 8 were used in this experiment, which was distributed in 2015 by Sibelco in Dordrecht. These sand packages were tested in dry conditions with a sieve machine at the faculty of Civil Engineering at University of Delft. The sieve experiment results of the three used grains are shown in the Particle Size Diagram shown in Figure 7.1. The details of the sieve tests are attached in Appendix A along with the manufacture sheets. Table 7.1 shows the results of the three sand packages with results of the D_{50}, density, porosity, internal friction and uniformity coefficient.

Each sand package was tested three times before the start of the experiment to ensure results as described in Appendix A. The content exists of non-cohesive sand from more than 98% of siliciumdioxide. These three sand packages were of a grey-ish color mixed with some white particles. The density in the dry state condition was for these three sand types $2630 kg/m^3$. The D_{50}, was obtained by linear interpolating.

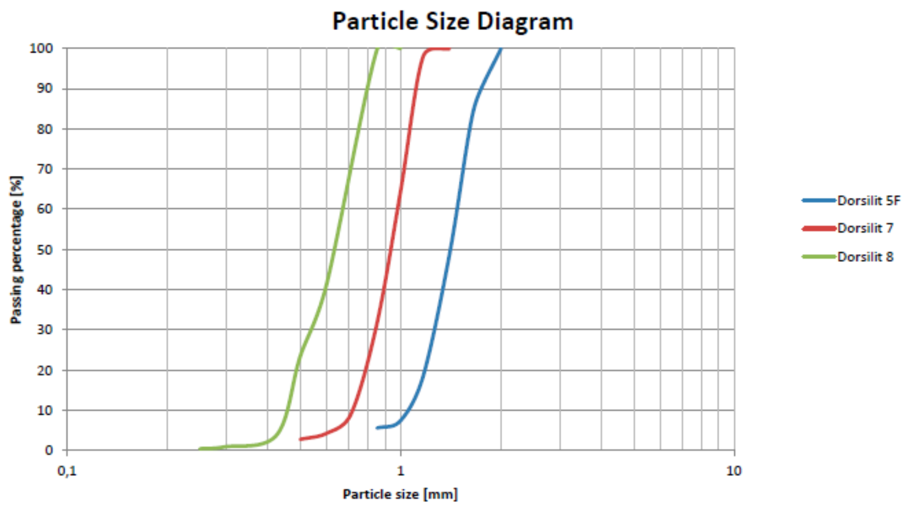

Figure 7.1: Particle Size Distribution

Type sand	Diameter $[mm]$	Density $[kg/m^3]$	Porosity [-]	Internal friction angle [°]	Uniformity coefficient $[-]$
Dorsilit 5F	1.41	1971.3	0.38	33	1.42
Dorsilit 7	0.93	1903.5	0.35	33	1.34
Dorsilit 8	0.63	1938.2	0.43	31	1.52

Table 7.1: Sieve result of sand

D_{50} has a little variation within the 10% margin from the prescript. The deviation is so small that the D_{50} in the Table A.11 will be used for further calculations in this study. The internal friction angle for sands was between the 31° and 33°, therefore particles can be classified as sub roundness.

Each sand package have an uniformity coefficient of 1.34 and 1.52. Sand is usually sorted at the manufacturer, since grains occurring in nature are mostly badly graded. Uniformity coefficients are valued near to one, which means that there is a higher permeability of sand soil.

7.1.2 Glass beads

The beads were used for this research as an artificial sand bed. The shape of each bead was assumed to be perfectly spherical and smoothly shaped. The manufacturer can produce beads with small error due to the reliable machines in controlled area.

Type Glass beads	Diameter $[mm]$	Internal friction $[°]$
Small	1.13	14
Large	1.45	13

Table 7.2: Sieve result of glass beads

Small and large glass beads have respectively a D_{50} of 1.13 and $1.45mm$ as shown in appendix A. The research equipment was insufficient to provide some accurate results. A large part of the beads got stuck in the two sieves, which analysing the diameter size difficult. The diameter was, therefore, assumed to be $D_{50} = 1.13mm$ and $D_{50} = 1.45mm$ as derived from the production sheets. The internal friction angels are respectively 14° and 13°. The solid density was $2500kg/m^3$ in dry state.

7.2 Flow characteristics of jet

Normal flows were tested with the stationary plain jet in impinging and free state before the main experiments were conducted with sand soil. The two gauges measurements would not vary too much, if a 3D effect is not present during the tests.

Two pressure gauges measured the flow field beneath the jet. Each run had a duration of one minute for impinging and free jet. During that time, the averaged and turbulent part has been recorded for the stagnation pressure.

7.2.1 Impinging jet

The detailed results of the stagnation pressure are shown in Table C.2 for impinging jet with its main and fluctuations values. Sensors were placed at

15 and 50mm length from the front panel at the impermeable flat surface for measuring various velocities and H/d distances. The pressure gauges were mounted in a flat smooth plate at the bed level, which were connected to a computer for measuring instant local stagnation pressure. Results for $SOD = 10$ are shown in table 7.3 along with the averaged and fluctuation values for several outflow velocities.

Velocity $[m/s]$	Front gauge $[kPa]$	Middle gauge $[kPa]$	Front fluctuation $[kPa]$	Middle fluctuation $[kPa]$	Difference [%]
1.2	0.62	0.64	0.10	0.09	3.2
1.6	1.17	1.21	0.17	0.22	3.4
2.0	2.12	2.16	0.27	0.34	1.9
2.4	2.58	2.65	0.29	0.43	2.7

Table 7.3: Stagnation pressure at $z = 15mm$ and $z = 50mm$ beneath the plain jet

The stagnation pressures from the middle gauge had larger values than the front gauge for all tests. The values had a maximum difference of 3.4%. A net momentum towards the front panel can be concluded, possibly because of small seepage between the impinging table and the front panel that caused pressure differences. Also, wall friction could affect the hydraulic propagation near the wall. But, the small normal flow can be neglected as the deviation percentage is small. The normal flow is neglected in all further tests since the difference between the middle and front gauges is small.

Velocity $[m/s]$	Front gauge $[kPa]$	Middle gauge $[kPa]$	Front fluctuation $[kPa]$	Middle fluctuation $[kPa]$	Difference [%]	Difference [%]
1.2	0.62	0.64	0.10	0.09	16	14
1.6	1.17	1.21	0.17	0.22	15	18
2.0	2.12	2.16	0.27	0.34	13	16
2.4	2.58	2.65	0.29	0.43	11	16

Table 7.4: Fluctuations around averaged pressure

The fluctuation term of velocity (u') decreased at a larger outflow velocity in a fully developed regime, yet the middle gauge shows more turbulence in absolute value. The turbulence is at least 11% of the average stagnation pressure. $\tilde{u_0}$ and u' is u_0 as stated in Chapter 2. Averaged plus peeks could trigger incipient motion of a single particle, if resistance is smaller than the hydraulic force.

$U_0 = 2.0m/s$ at H/d= [−]	Stagnation pressure [kPa]	Fluctuation pressure [kPa]	Difference [%]
10	2.16	0.34	16
20	1.22	0.31	25
30	0.86	0.12	14

Table 7.5: Stagnation pressure for impinging jet at several stand off distances

Three tests were done at SOD 10, 20 and 30 for one certain momentum outflow. Stagnation pressure correlates inversely with SOD, which is in line with the erosion parameter (equation 4.8). A larger SOD leads to smaller averaged stagnation pressure and fluctuations.

7.2.2 Free jet

The experiments were executed for the flow characteristics with free jet. Setting was almost similar as the impinging water jet, except that the impervious surface was removed. Water was free to propagates towards the bottom of the flume. Free jet can be seen as a 100% permeable bed without any blockage, although the small frontal area of gauge can have had a negative effect to the measured stagnation pressure.

Free jet has a vertical pressure difference beneath the plain jet. Normal flow is likely with larger averaged stagnation pressure in the middle gauge. This means a net force is present towards the front panel as in the impinging jet condition.

Fluctuation u' was also present in free jet in all outflow velocities during experiments. The instant stagnation pressure varied around 15% of the averaged value. The turbulence term (u') contributes the peeks for a short

Velocity $[m/s]$	Front gauge $[kPa]$	Middle gauge $[kPa]$	Front fluctuation $[kPa]$	Middle fluctuation $[kPa]$	Percentage Front-middle [%]	Percentage fluctuation [%]
1.2	0.76	0.77	0.10	0.10	13	13
1.6	1.16	1.13	0.18	0.19	16	17
2.0	2.10	2.14	0.24	0.26	11	12
2.4	2.51	2.56	0.43	0.48	17	19

Table 7.6: Stagnation pressure in normal directions for free jet

time, which might cause incipient motion for a single particle.

$U_0 = 2.0m/s$ at H/d= $[-]$ Free Jet	Stagnation pressure $[mm]$	Fluctuation pressure $[mm]$	Difference [%]
10	2.14	0.26	12
20	1.15	0.19	17
30	0.72	0.11	15

Table 7.7: Stagnation pressure for free jet at several stand off distances

The average pressure has an inverse correlation with SOD. The impinging distance-term is in line with the erosion parameter from the equation 4.8. The turbulence part makes up between 12 and 15% of the stagnation pressure.

Conclusion

No significant difference is observed in the turbulence term between the impinging and free jet. Free jet has a stagnation pressure in various outflow velocities and SODs.

- All stagnation pressures in the free flow were slightly lower than in the impinging jet.
- The average pressure at the stagnation point differed slightly from the middle and front gauge. The impinging jet indicated a 3.4% pressure

difference in normal directions, while the free jet had a deviation of 2.0% in normal directions.

- Fluctuation was observed at the averaged stagnation pressure at all outflow velocity around 15% for impinging and free jet.
- Stagnation pressure was inversely related to SOD. The correlation is in line with the erosion parameter.

7.3 Experimental results compared to similar tests

The bed dimensions of these experiments are compared to other similar tests. The goal for the comparison is to validate the plain jet and the sand bed geometry inside the flume. Detailed data are shown in Appendix D in the dynamic stable state. The results are processed in the Figures 7.2 to 7.4.

In the graphs, two lines can be observed. The red line represents the regression line of this research and the black line represents the results from a comparable experiments conducted by Rajaratnam [1981].

Cavity depth

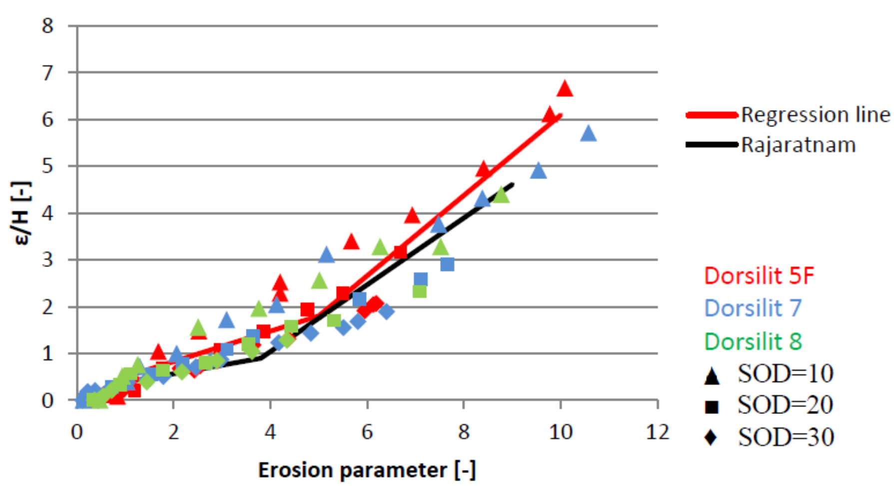

Figure 7.2: Jet erosion tests comparison to dimensionless depth

The data points seem to follow the trendline from Rajaratnam. Yet, some variations can be observed between 4.0 to 6.5 of the erosion parameter. The regression line has a transition point around the value 5.0, where the tangent of the cavity depth changes as well as the cavity width. The data points display some discrepancy compared to the trendline of Rajaratnam, which could be the result of the differences in grain properties, like roundness or chemistry content. The cavity width clearly differs at higher values of the erosion parameter. The report did not state clearly how Rajaratnam measured the cavity width, but the black trendline does seem to follow the experimental points from this study. Deviation in cavity width might causes by the limited dimension of the flume. It should also be noted that many observations from this experiment were in a wide range of erosion parameter.

The red regression line consists of the experimental observations with a transition point at erosion parameter 5.0. Dimensionless depth as a function of erosion parameter 1.0 until 5.0 is empirically defined as:

$$\frac{\epsilon}{H} = 0.29 * E_c + 0.211 \tag{7.1}$$

Dimensionless depth as function of erosion parameter from 5.0 is defined as:

$$\frac{\epsilon}{H} = 0.89 * E_c - 3.08 \tag{7.2}$$

Cavity width

The dimensionless width shows a similar trend as the function of erosion parameter, but the results display lower values along the erosion parameter. Results from Rajaratnam show almost similar results up to the value of 4.0. From that value on, the normalised width shows smaller values with higher values of the erosion parameter. One possibility could be the limited flume width, which affects the hydraulic flow pattern in the dynamic stable state. Secondary flow was not seen, but did affect the cavity growth.

The dimensionless cavity width is empirically correlated to the erosion parameter: Dimensionless width as a function of erosion parameter 0.4 until 5.0 is defined as:

$$\frac{\epsilon}{x} = 0.55 * E_c + 0.28 \tag{7.3}$$

Dimensionless width as function of erosion parameter from 5.0 is defined as:

$$\frac{\epsilon}{x} = 1.31 * E_c - 3.93 \tag{7.4}$$

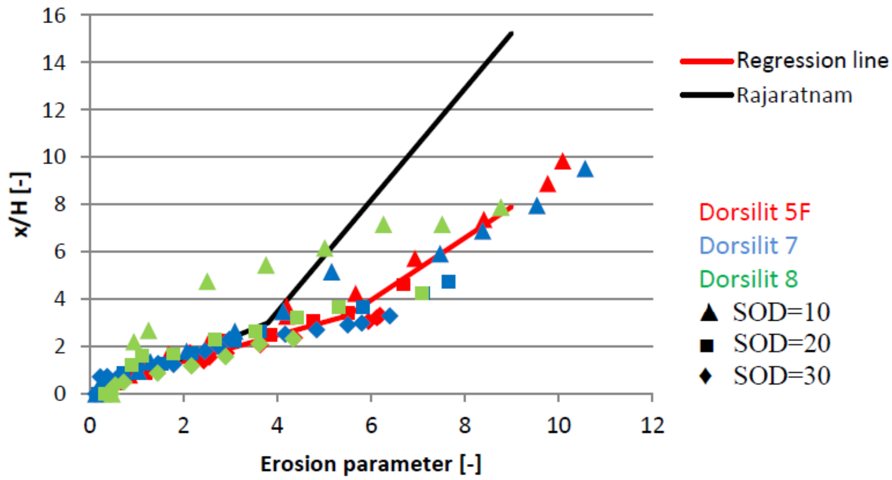

Figure 7.3: Jet erosion tests comparison to dimensionless width

Cavity hill height

The dimensionless hill height shows comparable results with other experiments conducted with plain jet. A small overestimation could be observed from the experiments until thee erosion parameter reaches 3.5, hereafter lower values than that of Rajaratnam can be observed. A clear transition is not observed around erosion parameter 5.0 from this research experiments. Overall, the absolute length of hill heights were relatively low.

The dimensionless hill height has a correlation with erosion parameter: The dimensionless hill height as a function of erosion parameter 0.5 until 5.0 is defined as:

$$\frac{\Delta\epsilon}{H} = 0.1 * E_c + 0.15 \tag{7.5}$$

The dimensionless hill height as a function of erosion parameter from 5.0 is defined as:

$$\frac{\Delta\epsilon}{H} = 0.28 * E_c - 0.83 \tag{7.6}$$

7.4 Reproducibility of the results

Test $D_{50} = 0.63mm$, $u_0 = 2m/s$ and $SOD = 10$ has been tested three times to check for reproducibility of the basic experiment. The test was conducted

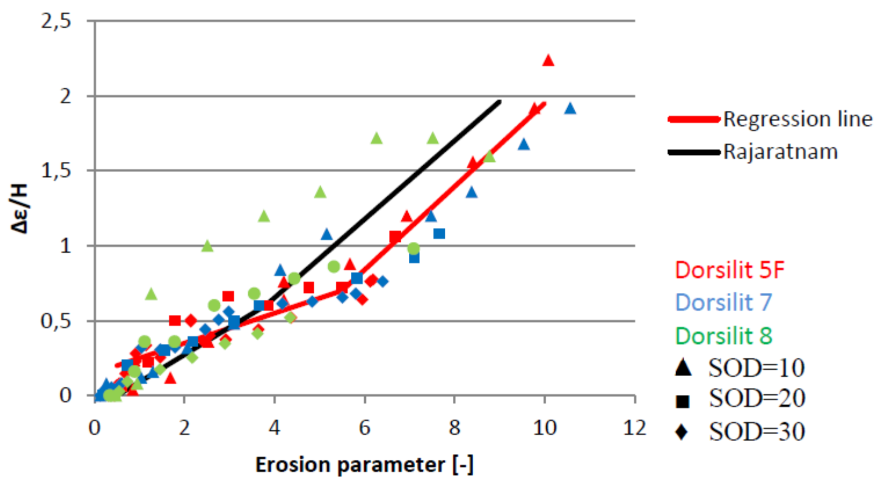

Figure 7.4: Jet erosion tests comparison to dimensionless hill height

to ensure the reliability and consistency of the submerged pump. As can be seen in equation 2.3, the turbulence term affects the reliability of the pump. The results from Table D.1 is shown in Figure 7.5.

The three lines in the graph show the observation points, which do not vary much from each other. The consistency of the pump is therefore verified with these three tests. Further experiments are therefore assumed to be consistent with representable outcomes for the specific test setting and the erosion velocity. The maximum deviation was at $t = 0.5s$ from the first and second tests.

7.5 Processes at bed in jet erosion test

This section described the observed processes at bed for a wide range of erosion parameter. Low erosion parameter values are discussed first. Then, higher values are considered.

7.5.1 Processes on bed at low erosion parameter

This test was conducted with an erosion parameter up to 1.0. Main characteristic is the low activity beneath the jet for the weak deflected jet.

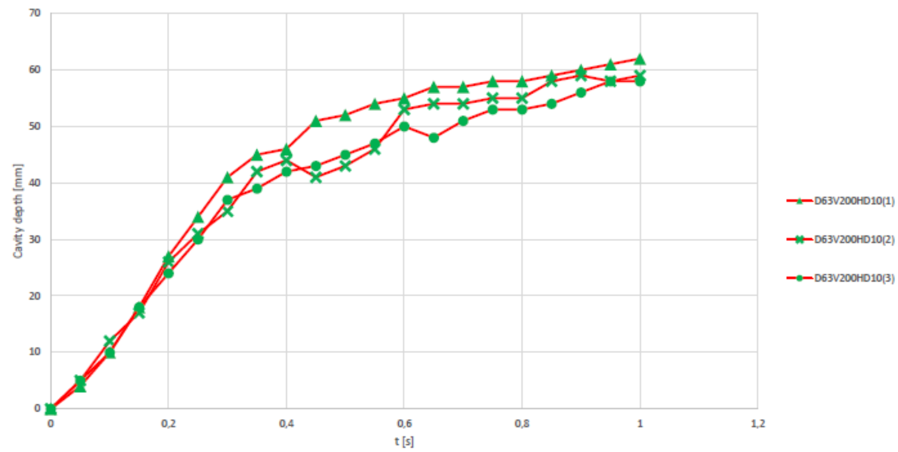

Figure 7.5: Consistency of the pump

At the start phase, the grains started rolling in lateral direction beneath the jet. The low momentum outflow let particles transport away from the centerline with a low take-off angle. Pick-up was likely triggered by micro hydraulic turbulence beneath the jet, because the particles were displaced over small distances. The cavity grows gradually to the final bed geometry. Recirculation of suspended grains started quickly, where entrainment is important to bring the particles back in the dynamic erosion. The suspended load is settled in the dynamic cavity after some time. Bed load transport was seen, if the bed eroded. Suspended load started along with bed load with an erosion parameter close to the value one for a while.

Particle movements stopped slowly to zero after some time. The suspended load is settled in the static cavity. Some times particles vibrated on the eroded cavity bed, this happened when hydraulic force is equal to resistance of the submerged particle. Cavity geometry shows a weak deflected jet with slopes smaller than the internal friction angle of particles.

At the end phase, the particles are all settled on the weak deflected cavity. The bed remains in the same geometry position after the pump has been switched off, so the the pick-up rate and particle transport were valued to zero. The stagnation point remained the deepest point of cavity in the test. Hills are formed with slopes equal to or smaller than the internal angle of the sand.

The pick-up rate was hard to measure, since singularity was observed around the stagnation point with individual particle movement. Pick-up

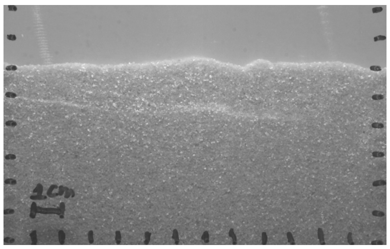

Before test

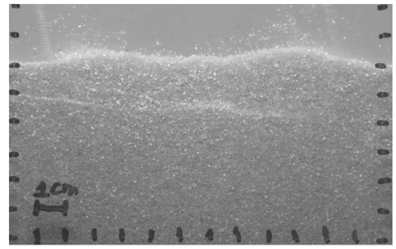

t=1.0s

Figure 7.6: Weak defected jet

rates were therefore too small to be determined.

7.5.2 Processes on bed at mid-range erosion parameter

In this test erosion parameter from 1.0 to 5.0 during the test. Main characteristic is the strong deflected jet with the pick-up in the inner cavity.

In the start phase, strong deflected jet showed soil deformation and surface erosion. Grains at stagnation point started pick-up with low take-off angle, similar to the test with low values of the erosion parameter. Micro turbulence is only a minor part of the pick-up in the start phase. In addition, large momentum from jet caused bed deformation at the bed as ejections. Grains were dragged along the curved cavity by the deflected hydraulic flow. An inner cavity appears with dynamic erosion in the outer cavity. Particles recirculate the suspended grains quickly after start, which effects the dynamics of turbulence in impinging jet. This is in line with the theory of Prandtl. Bearing capacity of soil was likely to be insufficient for the vertical force from the impinging plain jet. Calculation checks are also discussed int his section.

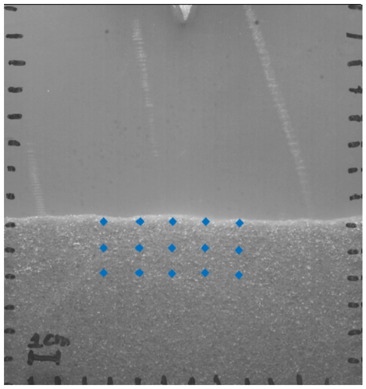

Initial bed condition

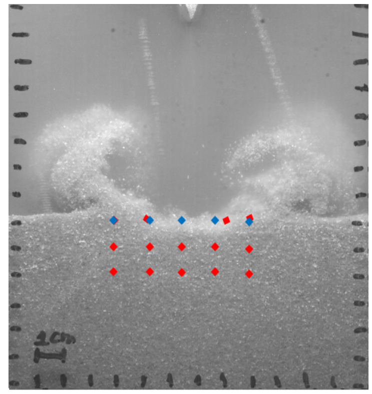

Bed condition at t=0.1s

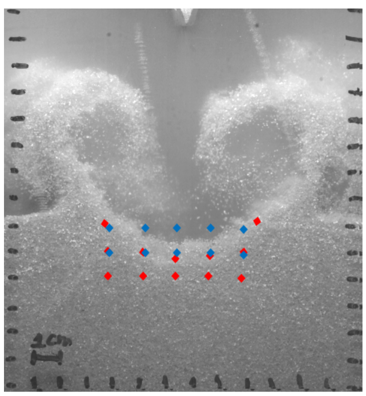

Bed condition at t=0.2s

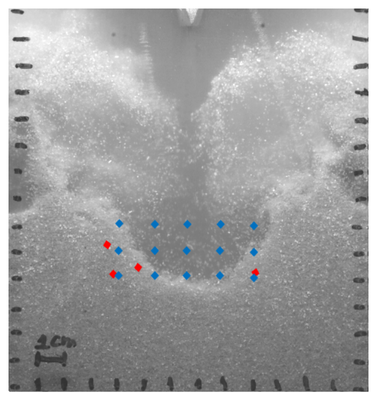

Bed condition at t=0.3s

Figure 7.7: Test 1 in start phase

In dynamic stable state, mid-range erosion parameter shows dynamic erosion above the inner cavity inside the outer cavity. A swaying stagnation point was observed at certain distances from the jet depending on the test settings. This was not seen in the start phase. The dominated hydraulic pressure stowed the inner cavity geometry to a more internal friction angle. The impinging jet on impervious bed tests showed the fluctuated stagnation pressure, which declares the dynamic stable cavity depth. At the same time, minor and dominant vortices switched frequently from side of the jet. The vortices seemed to want to break out from the jet. These sweeps could not propagate further in the stream, so the eye of the vortices distanced a certain distance from the jet. The dynamic inner cavity shape enclosed the vortices by the steep slope in the inner cavity, which exceeded the internal friction angle of the soil. The wall jet eroded in the inner cavity. The scoured flow separated at the transition of the inner and outer cavity. Active sliding sand bed added discontinuously bulk erosion to the jet system, which suspended the grains by the wall flow in the inner cavity. Small grains of the gradation were deposited at the outer slope, where the flow velocity is lower in the ambient water.

When the pump was switched off, dynamic erosion stopped instantly due to the lack of hydraulic force. Suspended grains were deposited on the bed by gravity. Steep inner cavity collapsed instantly because of absent of hydraulic force. The grains at the outer gravity rolled to the lower part of the cavity until the sand bed had reached its equilibrium. The dynamic stagnation point was covered with the suspended particles, which shortened the cavity depth compared to the asymptotic state. The deepest cavity point ends around the centreline but at a higher location. In contradiction, the settlement shortened the cavity hill height with a few millimeters from the original bed. The final bed had slopes with the internal friction angle.

Test case

Two test cases were checked for the bearing capacity, erosion rate and the pick-up rate in the mid-range of the erosion parameter.

The first test case has an erosion parameter with a value of 3.6. The jet has a $SOD = 30$ and the outflow velocity is $2.0m/s$.

The bearing capacity was measured from impinging jet $0.77kPa$. This value exceeds the bearing capacity of $0.26kPa$ from Prandtl's equation, which is in line with the observed soil failure. The assumption was made that 15% of vertical force would be in horizontal directions. Vertical movement is likely because of the insufficient bearing capacity of the soil. A zone III wedge could not be observed.

The graph shows the cavity depth development over time for both strong deflected and dispersing jet, which can also be seen as erosion velocity.

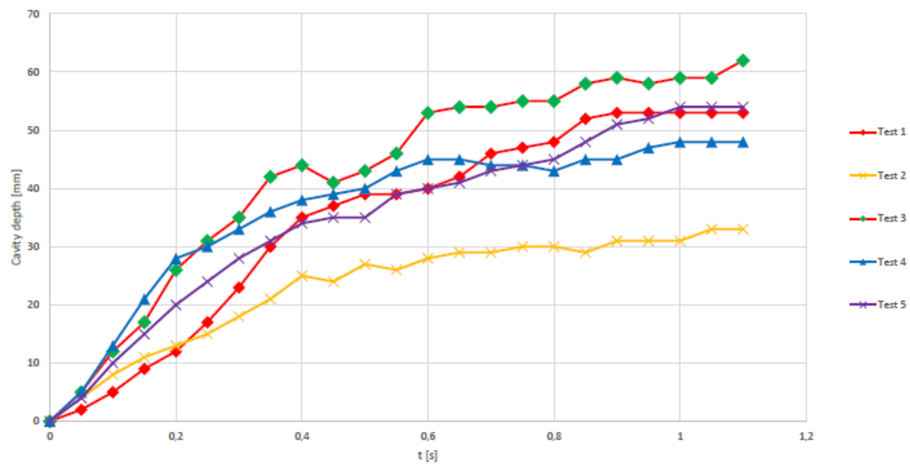

Figure 7.8: Cavity depth development in time

This test case is plotted as the red line with the diamond shapes.

The experimental pick-up rate was checked with the theories of Van Rijn, Meyer-Peter Müller and Van Rhee as shown in Figure 7.9.

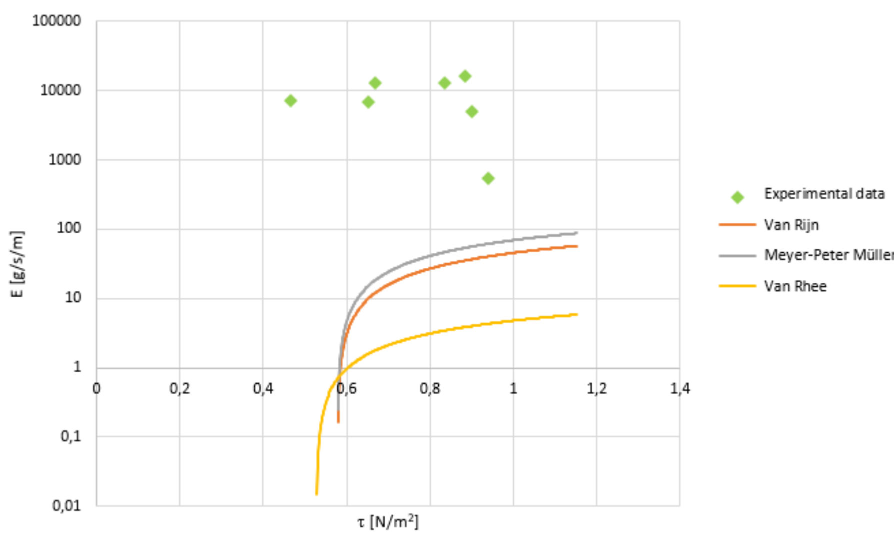

Figure 7.9: Pick-up rate from test 1

The pick-up rate from this experiment was with a factor ten larger compared to Van Rijn, Meyer-Peter Müller and Van Rhee. The erosion parameter was 3.6, but the pick-up rates were slightly larger. Pick-up rates were approximately $12000g/s/m$ with a small increase as a function of the shear stress. The propagating energy is reduced by viscous flow before hitting the sand bed. The momentum spread in the hydraulic mixing layer over a larger area beneath the jet.

The second test case had an outflow velocity of $1.2m/s$ with $SOD = 10$. The erosion parameter is 3.8 was comparable value of test case 1. The measured pressure is $0.64kPa$ from table 7.3. The theoretical bearing capacity is 0.26 calculated with equation 3.2. Vertical movement happened because of insufficient bearing capacity of the soil which was also observed this test.

The erosion velocity was in test 2 smaller than in test 1. Smaller jet momentum resulted in lower pick-up rate as in the yellow plot in Figure 7.8.

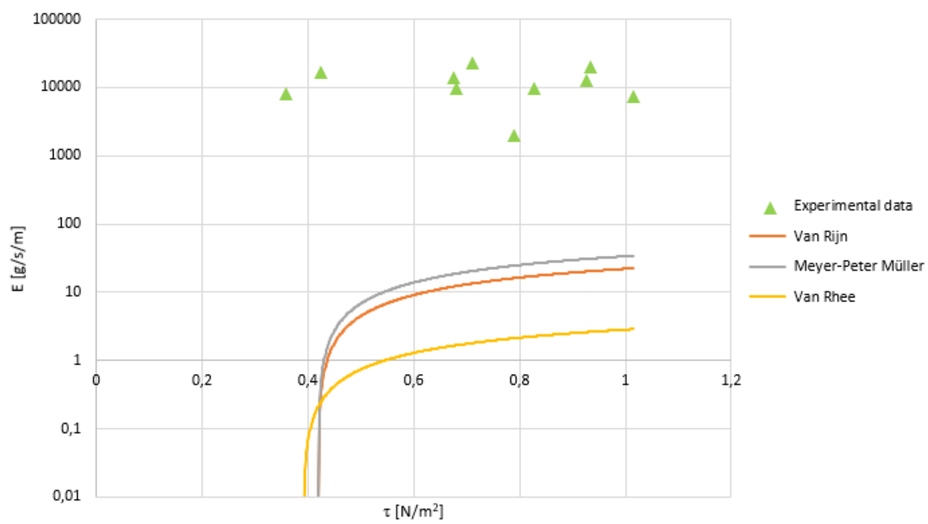

Figure 7.10: Pick-up rate from test 2

The pick-up rate from this experiment was with a factor ten larger compared to Van Rijn, Meyer-Peter Müller and van Rijn. Shear stress is likely not to be related to the pick-up rate. The erosion parameter was 3.8 with pick-up rate around $11000g/s/m$ regardless of the shear stress. The lower jet momentum has a lower pick-up rate than in test 1.

7.5.3 Processes on bed at large erosion parameter

Erosion parameter is treated from 5.0 till 10.6 for all the relevant processes during test. Main characteristic is the strong deflected jet with the pick-up in the inner cavity.

Dispersing jet showed bed deformation and surface erosion at the starting phase. High jet momentum hits the soil bed. Sand particles translated and rotated quickly in the bed in this regime after the start as showed in Figure 7.11. Ejections were observed because of insufficient bearing capacity according to Prandtl's theory. Turbulence caused that the sweeps got into deeper soil, which widens the cavity at the same time in the starting phase. The stagnation point was at $t = 0.1s$ to the right and at $t = 0.4s$ to the left. The plastic zone and the passive zone were seen on the videos just like in the theory of Prandtl. Soil wedge (zone III, see 3.1) beneath stagnation point could not be clearly observed. It could be possible that the turbulence on the bed surface diminished the force balance in the triangle. The inclination factor increased as described in Chapter 3.10. Recirculation of suspended grains started just milliseconds after the start. A shield of grains was formed above the dynamic erosion, which indicated insufficient erosion capacity for a short period of time. Cavity grows more in depth than under strong deflected jet.

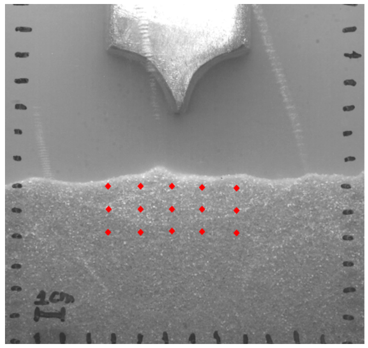

Initial bed condition

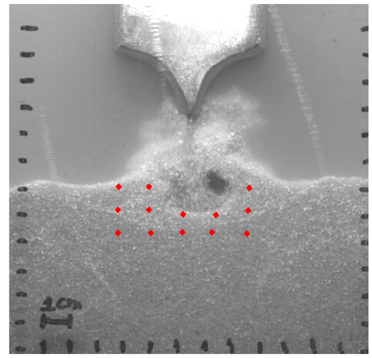

Bed condition at t=0.1s

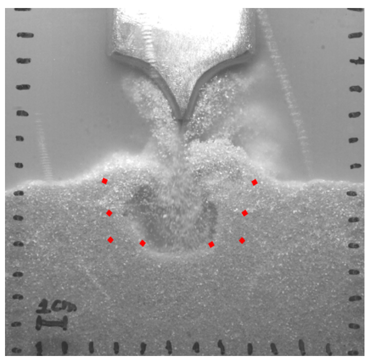

Bed condition at t=0.2s

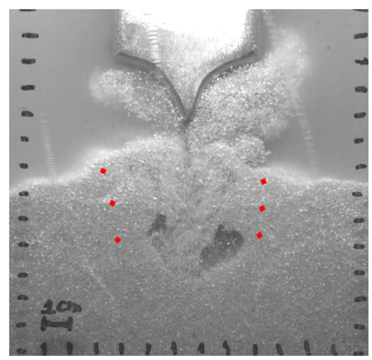

Bed condition at t=0.3s

Figure 7.11: Test 3 in start phase

Dispersing jet had a dynamic stable cavity after a while. Many similarities with strong deflected jet could be observed in this stage. A big difference is that the cavity depth-width ratio is larger in the dispersing jet condition. Dynamic erosion had a more chaotic flow pattern. The shield of particles above inner cavity had been disappeared before reaching this stage. Small gradation in particles were seen during these tests. Minor and dominant vortices switched continuously from one side of the center line. The minor vortex had a greater supply of grains from dynamic erosion, while the dominant vortex lost suspended particles. This activity switched from side when the minor vortex had a larger concentration of grains. Along the steep slopes eroded with the active soil failure as a sliding sand volume. Smaller particles could displace relatively over larger distance from center line by experiencing smaller drag forces, while larger grains deaccelerate faster by large frontal area during the transport.

Dynamic erosion stopped when the pump was switched off. Suspended grains deposited on the bed by gravity. Steep inner cavity collapsed along to lower part of the bed. The dynamic stagnation point was covered with the suspended particles, which shortened the cavity depth compared to asymptotic state. Settling was hindered, if high concentrations of grains fell down. The deepest cavity point ends at a higher location while the cavity hill height shortened with a few millimeters. The final bed had slopes with the internal friction angle of the sand soil.

Test cases

Test case 3 has a erosion parameter of 6.3 with outflow velocity of $2.0m/s$ in $SOD = 10$.

Maximum bearing capacity is $0.26kPa$ as calculated from equation 3.2. The measured stagnation pressure was $0.77kPa$ averaged over time. This value exceeds the maximum, which is in line with the bed deformation from observations.

The eroded depth was the largest of all analysed experiments. This means also the largest erosion velocity in the first second after start. Jet momentum is equal to that of test 1, but with a lower impinging distance. This is displayed as a red plot with triangle shapes in Figure 7.8.

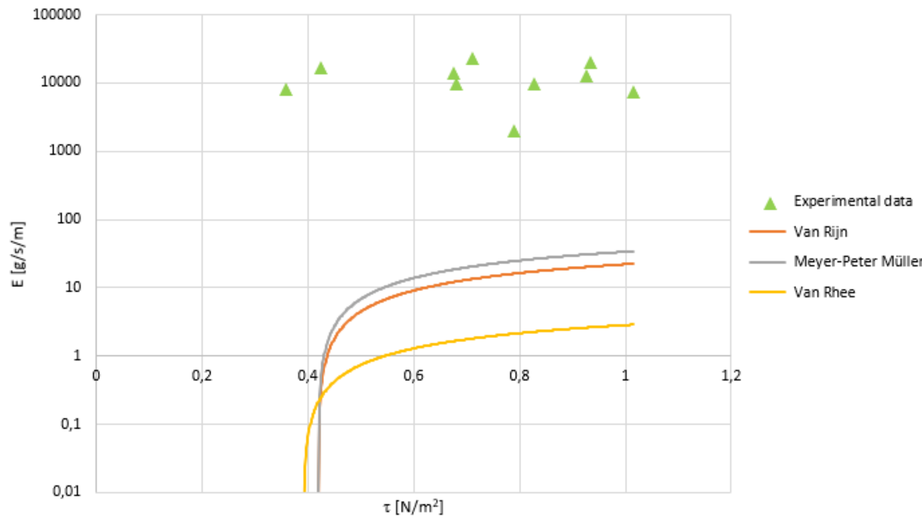

Figure 7.12: Pick-up rate from test 3

No considered theories can explain the results of the pick-up rates from this experiment. The theories underestimate the pick-up by a factor 100. The experimental rates are approximately $12000g/s/m$. Shear stress is larger at the starting phase compared to test case 1 with larger SOD and lower pick-up rate. Shear stress is apparently not a function of pick-up rate. The momentum outflow did not vary, so a likely correlation is made with the jet momentum and the pick-up rate.

Test case 4 has a bed with larger particles of D_{50} as in test 1. Grain size is increased from $0.63mm$ to $0.93mm$. The jet momentum is equal to test 1 and 3, but with an erosion parameter of 4.2.

Soil moved as Prandtl's theory explains because of insufficient bearing capacity. The measured stagnation pressure $0.77kPa$ exceeded the maximum bearing capacity of $0.25kPa$. A temporary shield grain was seen on top the cavity, which appeared by the small sediment discharge capacity.

The erosion velocity is similar as test 1 and 3 in the first $0.5s$. The same jet momentum resulted in the same order of erosion velocity. This displayed as the blue plot in Figure 7.8.

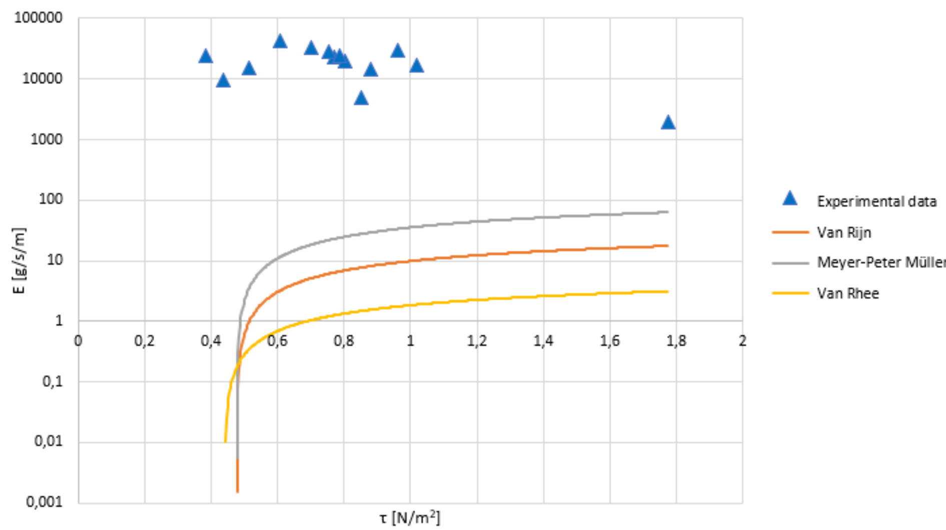

Figure 7.13: Pick-up rate from test 4

The experimental pick-up rates had larger values than what the theories prescribe. This considered test setting had the same jet momentum as test case 1 and 3. The erosion parameter is 5.2 with pick-up rates that were approximately $12000 g/s/m$ in the starting phase. In this test case, rates were slightly lower because of the larger grain size and larger weight than smaller particles. But still, jet momentum is a good indication of pick-up rate regardless of particle sizes.

7.6 Influence of density

Qualitative research was done for the loose and dense sand bed state from the plain jet. The interesting part was that density was not directly related to the erosion parameter, while permeability did correlate with density and erosion parameter. Also, a certain jet energy had to pick-up more particles per unit of eroded bed volume. A larger pick-up rate meant more turbulence along the propagating water stream, which resulted in a smaller cavity dimension. Erosion parameter should be smaller in dense bed state.

Test $[-]$	Depth dense $t = 1s$ $[mm]$	Depth dense $t = 2s$ $[mm]$	Depth dense $t = \infty$ $[mm]$	Depth loose $t = 1s$ $[mm]$	Depth loose $t = 2s$ $[mm]$	Depth loose $t = \infty$ $[mm]$
D63V040HD10	8	10	19	8	11	19
D63V120HD10	30	42	48	31	37	49
D63V120HD30	22	36	45	26	39	45
D63V200HD10	54	65	80	59	72	82
D63V200HD30	54	62	85	59	69	88
D93V120HD10	29	33	43	30	34	43
D141V120HD10	33	35	38	27	36	38
D141V120HD20	30	33	34	28	32	34
D141V120HD30	16	24	32	20	22	32
D141V200HD10	51	56	57	53	xx	57
D141V200HD20	48	52	54	49	53	54
D141V200HD30	41	43	46	43	45	48

Table 7.8: Initial deepening in dense bed compared to loose state

Overall, the penetration depth was smaller in the dense bed state than in the loose sand state. More recirculating particles reduced propagating momentum by turbulence toward the stagnation point. Less energy was available to infiltrate the sand bed for a deeper cavity. Cavity depth development takes a longer time to reach the asymptotic state as can be seen from Figure 7.8.

Test $[-]$	Width dense $t = 1s$ $[mm]$	Width dense $t = 2s$ $[mm]$	Width dense $t = infty$ $[mm]$	Width loose $t = 1s$ $[mm]$	Width loose $t = 2s$ $[mm]$	Width loose $t = \infty$ $[mm]$
D63V040HD10	54	58	69	48	52	67
D63V120HD10	116	122	140	102	120	136
D63V120HD30	112	152	182	114	142	176
D63V200HD10	150	196	366	122	174	358
D63V200HD30	196	xx	326	204	xx	318
D93V120HD10	108	136	138	106	126	132
D141V120HD10	61	67	96	51	56	92
D141V120HD20	66	71	80	67	72	77
D141V120HD30	72	81	82	65	76	78
D141V200HD10	78	80	96	70	xx	92
D141V200HD20	88	94	114	79	91	112
D141V200HD30	95	108	120	88	95	105

Table 7.9: Deepening in dense bed compared to loose state

The cavity width was larger in the first seconds in the dense sand conditions compared to when there was less packed sand soil. Possibly, the dense sand bed acted as an impermeable shield above vortices, which converted more longitudinal momentum to lateral directions by the hydraulic flow. Dense bed reduces the permeability, which is in line with the Shields parameter. The pick-up rate should be lower according to Van Rhee, which was not in line with the cavity width observations. The final cavity width has increased in the dense bed compared to loose bed state. The eroded soil volume was enlarged from packed bed to loose density at the bed level.

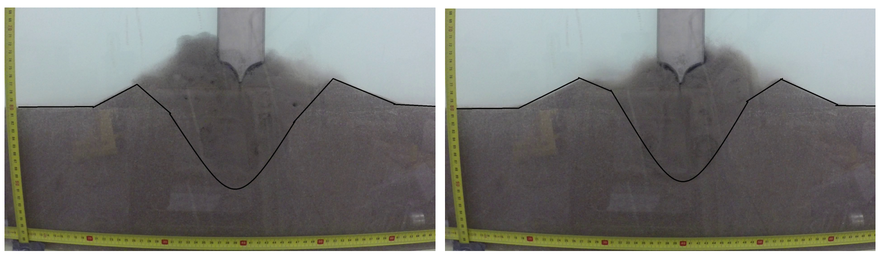

Test 3 in loose bed Test 6 in dens bed

Figure 7.14: Cavity in loose and bed state in dynamic stable state

The erosion parameter has no parameter for density, but bed geometry is in all cases different with dens soil. The cavity depth is just a few millimetres smaller, in contrary the cavity width is a few millimetres larger.

Test case 5

Test 5 had a higher density with similar jet setting like in test case 3. The density went from $1938.2 kg/m^3$ in loose state to $1994.5 kg/m^3$ in the saturated dense bed state. Porosity decreased from 0.43 to 0.38.

The erosion velocity is similar to that in test 1, 3 and 4 in the first $0.5s$. The same jet momentum resulted in the same order of erosion velocity. This is displayed as in the purple plot in Figure 7.8. The original dense bed state had less cavity depth in dynamic stable state.

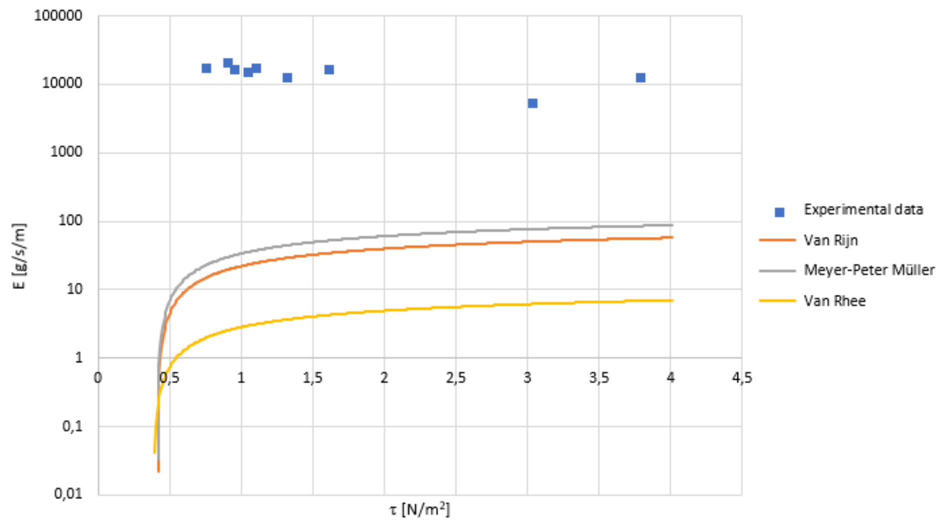

Figure 7.15: Pick-up rate from test 5(dense bed)

Actual pick-up rates were larger than the three considered erosion models. Shear stress is also not determinative in dens bed. The jet momentum is similar to that in test case 3. The pick-up rates were in the same order magnitude. The same amount of particles had to be displaced to reach a certain jet momentum, which leads to a smaller cavity dimension in the first second after the start. The cavity had slightly less depth in the dynamic bed state, but the width and hill heights were larger because of the increasing soil volume. Initial dense bed increased in volume to lose soil after deposition.

Conclusion

- A denser bed resulted to slightly smaller cavity depth, but a larger width. One unit of eroded dense soil had lower density after deposition, which widens the cavity.
- An eroded dense bed would turn into loose state after depositing on the original bed level. The loose deposition from a dense bed was larger than the original loose bed.

7.7 Influence of particle shape

Glass beads had effects on the dimensions of cavity. The comparison was made with large glass beads and Dorsilit 5F, that had a similar D_{50}.

The expectation would be that it would have the same eroded depth as sand soil. The cavity width and hill height are likely to be different, since the internal friction angle is smaller. Width would be larger and hill height smaller.

Test case 6

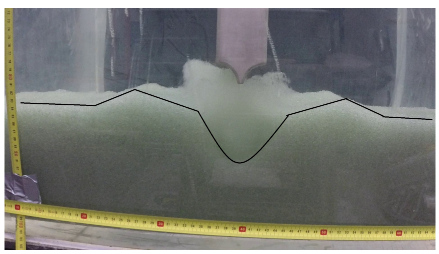

Figure 7.16: Test 6 with glass beads

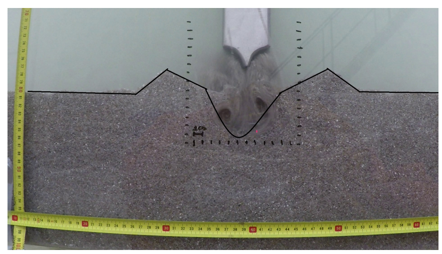

Figure 7.17: Similar test with sand

Beads beneath the jet started with surface erosion and bed deformation. Micro turbulence causes surface erosion in the start phase. Bed deformation was observed in line with the theory of Prandtl.

The bed geometry had some significant differences in dimensions. The cavity depth was deeper than the sand bed. This might be related to a lower solid density or the roundness of glass beads. The volume from the inner cavity had spread above the original bed level. Particles were deposited at the hills by impinging jet flow, while grains eroded to the lower part until the hill slopes take the internal friction angle of 13°. The hill height was clearly lower compared with sand soil. The dimension of the hills was much wider due to a lower internal friction angle than sand grains.

Transport could hardly be observed on camera. No clear figures could be made for the processes of glass beads. Pick-up rate for glass beads was analysed for that reason.

Two theoretical processes are important to the pick-up rate of glass beads compared to sand soil. Firstly, the shape of the glass beads reduces the resistance between particles because of a smaller contact area, which increases the pick-up rate around the stagnation point. Secondly, the skin friction of the beads decreases the hydraulic drag coefficient, which reduces the pick-up easier.

7.8 Influence of permeability

Dry sand volume was mixed with 6.0% bentonite. Conversion to dry mass has been applied, which meant a 3.6% mass percentage of dry sand. This percentage did block the permeability, but it will not behave as silt. Sand and bentonite were mixed well manually in dry condition. A small portion is spread evenly in the dry flume to a height of $0.20m$. The flume is slowly filled with water to avoid any stirring and turbidity. The actual execution of the test happened after resting 24hours, so that the bentonite could bulge with water between the sand particles. The mixture reduces the permeability to 90% compared to the sand bed.

The expectation was that the bentonite mixture will erode on the surface beneath the jet. Dilation is important, since voids are locked up. Bed deformation will immediately be blocked by the underpressure in void space. The pick-up rate was expected to be smaller. Van Rhee relates the permeability as inverse to the Shield parameter (eq. 4.26). The pick-up is correlated inversely with Shield, so a smaller permeability should lead to a reduction in the pick-up rate. Surface erosion would be expected by micro turbulence, but critical shear stress is higher because of stickiness between the particles. Sand bed might erode as chips if cohesiveness is high with a large hydraulic force.

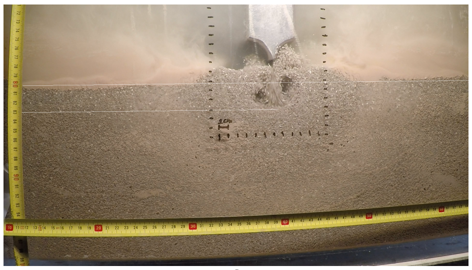

Bentonite flow in bed

Clear water from bentonite mixture

Figure 7.20: Permeability in soil bed

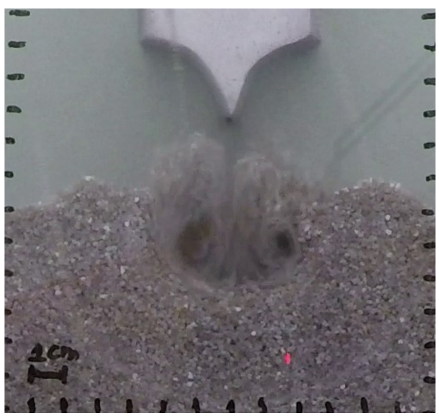

Figure 7.18: Sand soil without bentonite

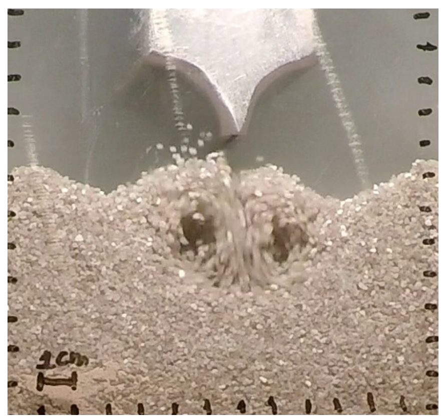

Figure 7.19: Mixture of sand and bentonite

The results were not as expected, the cavity geometry in bentonite was larger than the non-cohesive sand soil after twenty minutes. The permeability and stickiness should increase the resistance between the particles and lead to smaller cavity. The contradiction was observed a larger cavity depth, width and hill height as can be seen in Figure 7.18 and 7.19. The pick-up rate was larger, which contradicts with the lower permeability and the lower pick-up rate. The soil bed compacted as loose sand into dens bed with appearance of small ejection. Possibly the valve was not set correctly. A larger momentum leads unfortunately to a larger cavity geometry.

Ground water flow was observed, which was assumed to be zero, which is visible with concentrated bentonite as a pressure wave after start as in Figure 7.20. The wave moved with around $0.1m/s$ through sand bed for seconds. After some time, the concentration was diluted with clear water.

Test case 7

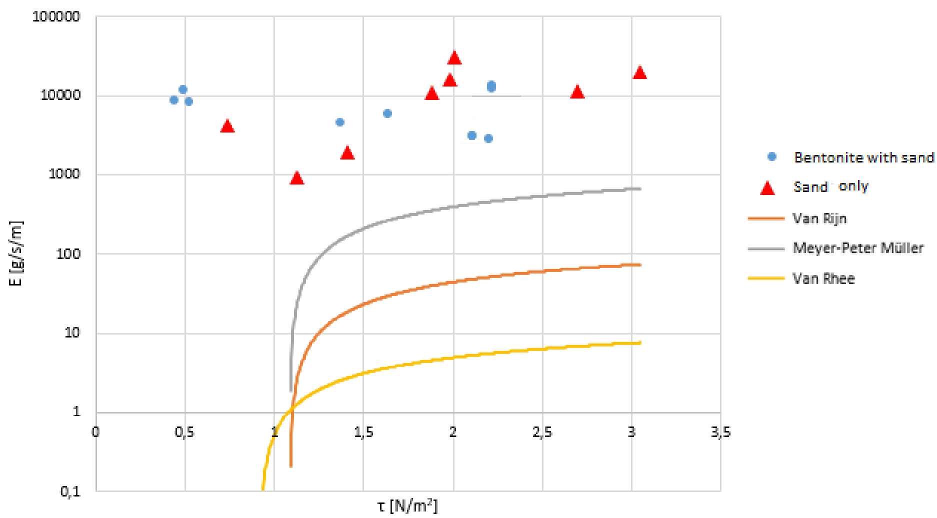

Figure 7.21: Pick-up rate comparison with bentonite mixture and sand only

The pick-up rate was surprisingly higher with bentonite soil than without at the starting phase. The dimensions of the cavity were larger for depth, width and hill height in the dynamic stable state. It could be possible that the mixture test setting was configured wrongly with a higher fluid outflow. A larger cavity geometry indicated a higher jet momentum from the impinging jet during the experiment. The consequence was a larger pick-up rate because of larger outflow energy at the starting phase.

7.9 Momentum as function of pick-up rate

One of the hypothesis is the pick-up rate as function of jet momentum. This is shown in Figure 7.22.

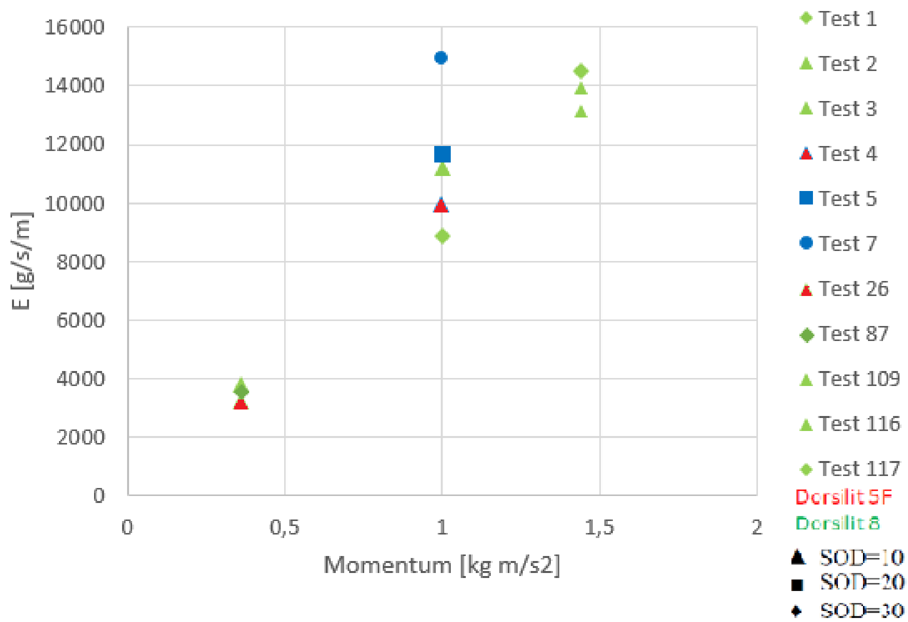

Figure 7.22: Pick-up as function of jet momentum

Similar jet momentum had almost the same magnitude of pick-up rate in the start phase. This proved the strong correlation between the jet momentum and the pick-up rate. The jet momentum determined the pick-up rate. Parameters like grain sizes and SODs had not a significant effect to the pick-up rate. Larger jet momentum resulted in larger deviation in pick-up rate. The pick-up flux decreased with the increasing jet momentum. Hindered erosion reduced the growth in the erosion velocity.

Dens bed (test 5) showed a slightly larger pick-up rate as for the loose bed. Same energy outflow had moved more amount of solid particles. The specific energy was lower for the solids, despite that the pick-up was larger for the dense bed.

Chapter 8

Conclusion and recommendations

8.1 Conclusion

The following conclusions can be made from the experiments in the laboratory:

- The first grain movement was a surface erosion beneath the jet in all jet erosion tests caused by turbulences inbetween the two vortices. The instant shear stress eroded soil bed into a weak deflected jet. The turbulence varied the shear stress in time, so the stagnation point was swaying beneath the jet. A small hill was not formed inside the cavity as in my hypothesis as in Figure 6.2 for all experiments.
- Erosion parameter from 1.0 showed strong deflected jet with pick-up inside the inner cavity. Ejection and bed deformation was the main causation of the cavity pick-up. The turbulence caused sweeps for sediment motion beneath the jet, which resulted in instant shear stress on the soil bed. Bed and suspended load followed above the dynamic bed geometry as injection. The momentum on bed from the jet exceeded the bearing capacity from the theory of Prandtl, which translated and rotated the particles in the bed in the start phase. The occurrence was soil failure.
- Pick-up rate was correlated to the jet momentum. The experimental tests showed a fixed jet momentum result in a pick-up rate with weakly dependency with SOD and grain size. Jet momentum caused bed deformation, if maximum bearing capacity was exceeded. Particle translation mainly determined the pick-up rate.

- Erosion theories are underpredicted the pick-up rate for the jet erosion tests. Soil failure is because of the loading exceeding the bearing capacity.
- Dense soil bed should be corrected for the permeability. Pick-up rate was smaller than in the original dens bed by higher resistance between particles compared to the loose bed.
- Similar tests to that of Rajaratnam were reproduced with experimental JET in non-cohesive soil. Cavity depths and hill heights were similar, but the cavity widths were significant lower for the larger values of the erosion parameter.

8.2 Recommendation

- Normal flow was measured with gauges in the validation phase. This means a small normal net force is present beneath the plain impinging jet, while the focus was 2-dimensional. A jet without front casing could avoid the normal water flow.
- The dimensionless width as function of the erosion parameter differs from similar tests. Hence, tests with a wider flume is recommended for preventing secondary flow, which might have affected the cavity width.
- The test with bentonite mixture has a larger cavity dimensions than a normal sand bed. This could not be clarified. The jet momentum was likely larger because of wrong test settings. Accurate outflow settings are recommended to get a good result.

Bibliography

M.L. Alberson, W.D. Baines, D. Citrini, S. Corrsin, Y.B. Dai, H.R. Henry, J.S. Holdhusen, R.A. Jensen, H. Rouse, and A. Streiff. Diffusion of submerged jets-discussion. *TRANSACTIONS OF THE AMERICAN SOCIETY OF CIVIL ENGINEERS*, 115:665–697, 1950.

J.A. Battjes. Vloeistofmechanica. *Collegedictaat CT2100*, 2002.

F. Bisschop. Erosion of sand at high flow velocities. 2018.

H.J. de Vriend, H. Havinga, B.C. van Prooijen, P.J. Visser, and Z.B. Wang. River engineering. *Collegedictaat CIE4345*.

H.B. Fischer, J.E. List, C.R. Koh, J. Imberger, and N.H. Brooks. *Mixing in inland and coastal waters*. Elsevier, 2013.

B. Foortse. Retardation of breach growth under high flow velocities. 2016.

J.W. Gauntner, P. Hrycak, and J.N.B. Livingood. Survey of literature on flow characteristics of a single turbulent jet impinging on a flat plate. 1970.

A. Koched, M. Pavageau, and F. Aloui. Vortex structure in the wall region of an impinging plane jet. *Journal of Applied Fluid Mechanics*, 4(2), 2011.

W.F. Molenaar and M.Z. Voorendt. Manual hydraulic structures 1. *Collegedictaat CIE3330*, 2012.

I. Nezu, A. Tominaga, and H. Nakagawa. Field measurements of secondary currents in straight rivers. *Journal of Hydraulic Engineering*, 119(5):598–614, 1993.

N. Rajaratnam. *Turbulent jets*, volume 5. Elsevier, 1976.

N. Rajaratnam. Erosion by plane turbulent jets. *Journal of hydraulic Research*, 19(4):339–358, 1981.

C. van Rhee. Dredging processes 2. *Collegedictaat COE4727*, 2015.

C. van Rhee and A. Bezuijen. Influence of seepage on stability of sandy slope. *Journal of geotechnical engineering*, 118(8):1236–1240, 1992.

L.C. van Rijn. Sediment pick-up functions. *Journal of Hydraulic engineering*, 110(10):1494–1502, 1984.

G.J. Schiereck. *Introduction to bed, bank and shore protection*. CRC Press, 2003.

A. Verruijt and S. van Baars. *Soil mechanics*. VSSD Delft, the Netherlands, 2007.

Appendix A

Grain size analysis

This appendix chapter is aimed to support the main body of this report with a particle sieve analysis conducted at the faculty Civil Engineering in Delft. The first part of this chapter describes the properties of the respective sand, which was ordered at the company Sibelco Europe located at Papendrecht in the Netherlands. The second part is about the characteristics of glass beads that were also sieved in the laboratory. This material was bought from the firm Sigmund Lindner GmbH located in Germany.

Method

The diameter of the sieves are chosen based on that mesh sizes are around the same D_{50} as described on the product sheet. Each sieve and dustpan are weighted before the sieving tests start. The sieves with the largest mesh piles up at the top of the sieve column. Smaller grain openings are placed lower in the sieve column. A dustpan is placed to obviate the very small particles between the sieve column and apparatus. The sand bag is mixed well before it is put into the sieve machine. The machine shakes for ten minutes, so grains can fall through the sieves. The mass of each sieve and dustpan are weighted with the filtered particles inside. The result can be proceed for the particle sieve analysis.

Each soil package is tested three times to ensure reliable results. The measured weights are noted to proceed the cumulative mass and passing cumulative mass percentage. A graph shows the grain diameter on the horizontal log-axis and the cumulative relative mass on the vertical axis. The analysis is also repeated for the other two sand volumes and two other different glass beads.

The weight of each batch is then compared to see, whether the error is within the 1% before and after each run, to ensure reliable sieve results. The outcome is the average weight of each particle package from the three tests, which uses for a proper semi-log graph for each soil volume. Another method is linear interpolating of the two nearest data points for the D_{50} in the semi-log graph.

Procedure:

- Read D_{50} sand from production sheet
- Choose several sieves around D_{50}
- Measure mass of each empty sieve
- Take a volume sand
- Measure the mass of the volume sand
- Place the sieves correctly on the sieving apparatus
- Start the machine and set the timer to 10 minutes
- Wait
- For each sieve layer measure the mass
- Calculate the genuinely particle mass of each sieve
- Show results in table and graph

Sieving results: Dorsilit 5F

The sand Dorsilit 5F comes from crystal silica sands. The material is packed in a bag of around $25kg$ each. Sand particles are sub rounded with gray-ish color and compose about 99.1% of silicon dioxide (SiO_2). The solid density is $2630kg/m^3$. The production sheet (page A9) shows that the majority of the grains should be between 1.0 and $1.8mm$. Therefore, sieves with these meshes were chosen: 0.85, 1.0, 1.168, 1.4, 1.6, 1.7, and $2.0mm$.

The D_{50} is $1.43mm$, which was determined by linear interpolating the points between 1.4 and $1.6mm$. The determined value fitted well with the production sheet from the manufacturer. The internal friction was about 33° with loose saturated density of $1971.2kg/m^3$ for this sand batch. The uniformity coefficient is determined by linear interpolation, $C_u = \frac{D_{60}}{D_{10}} = \frac{1.477}{1.039} = 1.42$. Dorsilit 5F is classified as poorly graded soil with almost similar grain size.

Sieve	Sieve diameter [mm]	Test 1 [g]	Test 2 [g]	Test 3 [g]	Average mass[g]
1	2.0	0.3	0.2	0.3	0.3
2	1.7	70.4	59.6	74.2	68.1
3	1.6	50.1	44.9	60.3	51.8
4	1.4	163.2	152.7	186.4	167.4
5	1.168	148.3	159.4	196.7	168.1
6	1.0	52.4	59.6	72.0	61.3
7	0.85	8.5	11.0	12.1	10.5
8	dustpan	25.3	44.5	23.8	31.2
	total	518.5	531.9	625.8	558.7

Table A.1: Sieve results with Dorsilit 5F

Sieve	Sieve diameter [mm]	Average mass [g]	Cumulative mass [g]	Passing cumulative mass percentage [%]
1	2.0	0.3	0.3	99.9
2	1.7	68.1	68.4	87.8
3	1.6	51.8	120.2	78.5
4	1.4	167.4	287.6	48.5
5	1.168	168.1	455.7	18.4
6	1.0	61.3	517.0	7.5
7	0.85	10.5	527.5	5.6
8	dustpan	31.2	558.7	0

Table A.2: Particle sieve analysis with Dorsilit 5F

The fall velocity is around the range of 1.95 to 3.99 seconds, which means the particles have a diameter of 4.3 and 1.04mm. The earlier found D_{50} corresponds within these values.

Sieving results: Dorsilit 7

Dorsilit 7 is crystal silica sand, which is packed in shrink foil of around 25kg each. Sand particles are sub rounded with gray and white particle color and composes around 99.1% of silicon dioxide. The production sheet on page A9 shows that the grain sizes should be between 0.6 and 1.2mm. Sieves were

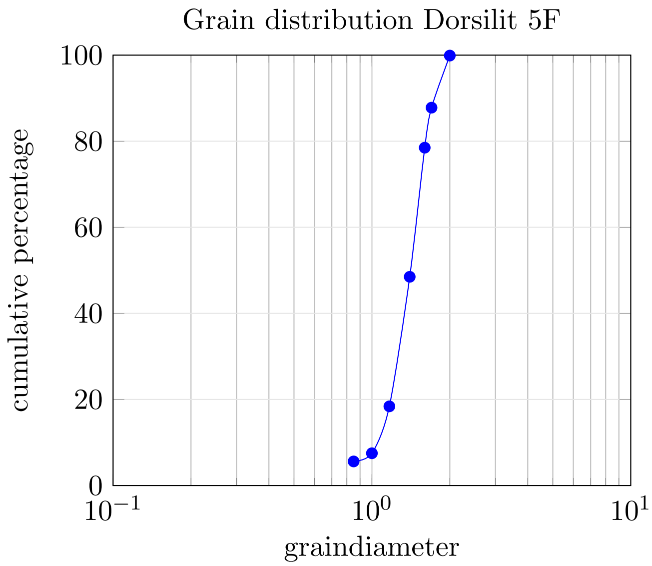

Figure A.1: Grain distribution Dorsilit 5F

used for particle size distribution with meshes 0.5, 0.6, 0.71, 0.85, 1.0, 1.168 and 1.4mm.

Sieve	Sieve diameter [mm]	Test 1 [g]	Test 2 [g]	Test 3 [g]	Average mass [g]
1	1.4	0.6	0.6	0.7	0.6
2	1.168	11.0	9.1	12.2	10.7
3	1.0	183.7	174.6	190.4	182.9
4	0.85	180.4	174.7	183.7	179.6
5	0.71	125.7	115.8	130.3	123.9
6	0.6	26.4	25.3	27.5	26.4
7	0.5	9.5	8.5	8.5	8.3
8	dustpan	18.7	14.5	12.5	15.2
	total	556.0	523.1	565.8	547.6

Table A.3: Sieve results with Dorsilit 7

According to the manufacturer the sub round grain diameter should be between 0.6 and 1.2mm. Linear interpolation is applied to two surrounding data points. Resulting in D_{50} of 0.93mm, which is a reasonable value and it

Sieve	Sieve diameter $[mm]$	Average mass $[g]$	Cumulative mass $[g]$	Passing cumulative mass percentage [%]
1	1.4	0.6	0.6	99.9
2	1.168	10.7	11.3	97.9
3	1.0	182.9	194.2	64.5
4	0.85	179.6	373.8	31.7
5	0.71	123.9	497.7	9.1
6	0.6	26.4	524.1	4.3
7	0.5	8.3	532.4	2.8
8	dustpan	15.2	547.6	0

Table A.4: Particle sieve analysis with Dorsilit 7

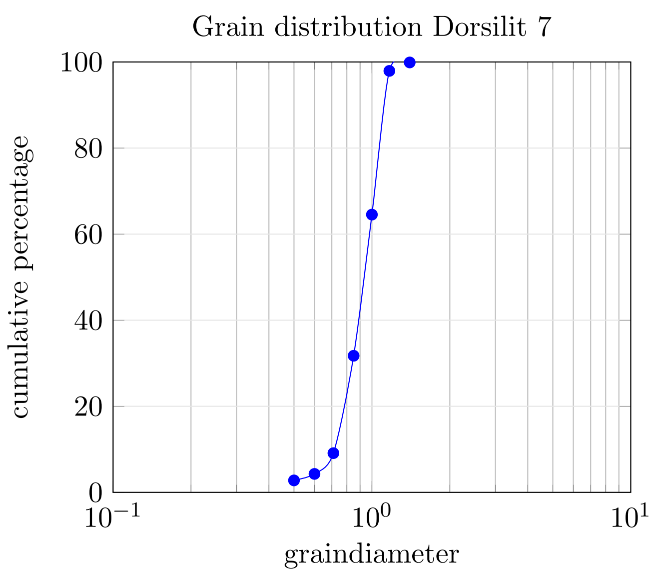

Figure A.2: Grain distribution Dorsilit 7

will be used in further investigations. The internal friction is 33°. The loose saturated density is $1903.5kg/m^3$ in dry solid state. Uniformity coefficient is $C_u = \frac{D_{60}}{D_{10}} = \frac{0.979}{0.730} = 1.34$, which means the regarding sand package is graded as poorly graded soil.

The fall velocity is approximately between the 2.26 and 5.14 seconds, which means the particles have a diameter of 3.2 and $0.62mm$. The earlier found D_{50} corresponds with these values.

Sieving results: Dorsilit 8

Dorsilit 8 contains crystal silica sand, which is packed in bags of around the $25kg$ each. Properties of sand particles are sub rounded with gray and white particle color and composes around 98,9% of silicon dioxide, according to the manufacturer's description. The production sheet (page A10) shows that the grain sizes has to be D_{50} around $0.57mm$. Sieves were chosen with meshes 0.125, 0.25, 0.297, 0.425, 0.5, 0.6, 0.85, and $1.0mm$.

Sieve	Sieve diameter [mm]	Test 1 [g]	Test 2 [g]	Test 3 [g]	Average mass [g]
1	1.0	0.2	0.1	0.0	0.1
2	0.85	1.3	1.3	0.7	1.1
3	0.6	354.9	307.6	287.2	316.6
4	0.5	94.4	104.2	93.3	97.3
5	0.425	102.0	114.6	102.0	106.2
6	0.297	16.9	17.1	14.2	16.1
7	0.25	2.7	2.7	2.5	2.6
8	0.125	2.4	2.0	2.1	2.2
9	dustpan	0.0	0.2	0.3	0.2
	total	574.8	549.8	502.3	542.4

Table A.5: Sieve results with Dorsilit 8

The D_{50} is $0.63mm$ after interpolating between the 0.6 and $0.85mm$ sieves. The sieved D_{50} is slightly larger than the prescript, the deviation is within the 10%. This error could have several reasons, it could e because of inaccurate test equipment or the manufacturer could have used different parts of their bulk volume. Sorting of grains diameter are unavoidable during processes or transportation. The deviation is not remarkably large and is assumed to have only little influence to the main results. The internal friction is $31°$ with loose saturated density of $1938.2kg/m^3$. Uniformity coefficient is $C_u = \frac{D_{60}}{D_{10}} = \frac{0.680}{0.448} = 1.52$. Dorsilit 5F is classified as poorly graded soil.

The fall velocity is around between the 2.49 and 7.50 seconds, which

Sieve	Sieve diameter [mm]	Average mass [g]	Cumulative mass [g]	Passing cumulative mass percentage [%]
1	1.0	0.1	0.1	99.9
2	0.85	1.1	1.2	99.8
3	0.6	316.6	317.8	41.4
4	0.5	97.3	415.1	23.5
5	0.425	106.2	521.3	3.9
6	0.297	16.1	537.4	0.9
7	0.25	2.6	540.0	0.4
8	0.125	2.2	542.2	0.04
9	dustpan	0.2	542.4	0

Table A.6: Particle sieve analysis with Dorsilit 8

means the particles have a diameter of 2.6 and 0.29mm. The earlier found D_{50} corresponds to these values.

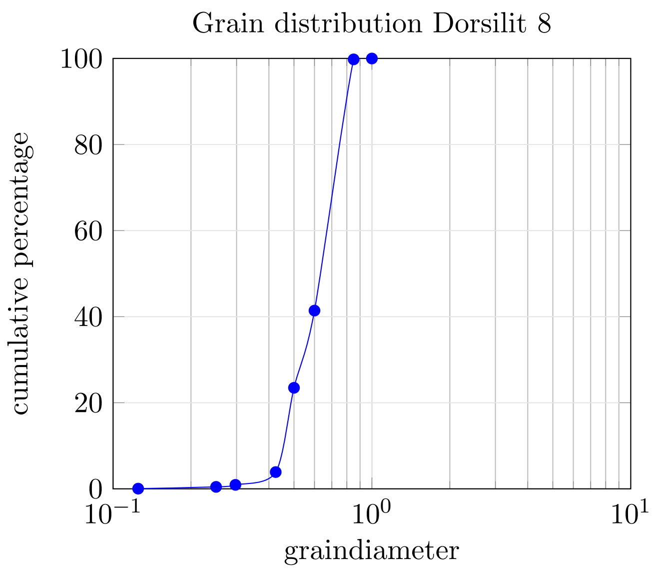

Figure A.3: Grain distribution Dorsilit 8

Technical Data

Dorsilit
Kristal kwartszand

Omschrijving

Dorsilit kristal kwartszand is een gewassen zand die zich door een hoog SiO2 gehalte en afwezigheid van humusachtige stoffen en andere verontreinigingen onderscheid. Na het drogen wordt het nauwkeurig uitgezeefd.

Toepassing

Dorsilit kristal kwartszand is onder andere geschikt als vulstof en instrooimateriaal voor kunststofgebonden troffel- en gietvloeren.

Eigenschappen

Vorm	:	rondvormig
Kleur	:	grijs / wit / gebroken wit / beige
Hardheid	:	7 Mohs
Soortelijk gewicht	:	2,63 kg/dm^3
Stortgewicht	:	1,60 kg/dm^3

Chemische Analyse
(Slechts een indicatie)

SiO_2	:	99,1 %
Al_2O_3	:	0,42 %
Fe_2O_3	:	0,024 %
TiO_2	:	0,020 %
CaO	:	0,02 %
MgO	:	0,02 %
K_2O	:	0,13 %
Na_2O	:	0,01 %
Gloeiverlies	:	0,20 %

Korrelmaten

Nr. 2F	3,0 – 5,0 mm	Nr. 7	0,6 – 1,2 mm
Nr. 3	2,0 – 3,5 mm	Nr. 8	0,3 – 0,8 mm
Nr. 5G	1,6 – 2,5 mm	Nr. 9	0,1 – 0,5 mm
Nr. 5F	1,0 – 1,8 mm		

Andere korrelmaten op aanvraag

Verpakking

- In plastic zakken van 25 kg op eenmalige pallets van 1000 kg met krimpfolie.
- Geweven polipropyleen big bags
- Losgestort in bulkauto

Bovenvermelde informatie is gebaseerd op gemiddelde waarden. De typische eigenschappen en chemische analyses zijn bedoeld als voorbeelden en kunnen niet beschouwd worden als vervanging voor eigen testen en onderzoek in alle omstandigheden waarbij eigenschappen en chemische samenstellingen kritische factoren zijn.

Neem contact met ons op voor meer informatie:

Worldwide
Tel: +31 (0)78 6546770
sales.eurogrit@sibelco.com

www.sibelco.eu

Sibelco Europe
PO Box 184
NL-3350 AD Papendrecht
The Netherlands

www.eurogrit.com

SIBELCO EUROPE

Technical Data

Dorsilit 8
Kristal kwartszand

Omschrijving	Dorsilit kristal kwartszand is een gewassen zand die zich door een hoog SiO_2 gehalte en afwezigheid van humusachtige stoffen en andere verontreinigingen onderscheid. Na het drogen wordt het nauwkeurig uitgezeefd.
Toepassing	Dorsilit kristal kwartszand is onder andere geschikt als vulstof en instrooimateriaal voor kunststofgebonden troffel- en gietvloeren.

Eigenschappen

Vorm	:	rondvormig
Kleur	:	grijs / wit / gebroken wit / beige
Hardheid	:	7 Mohs
Soortelijk gewicht	:	2,63 kg/dm^3
Stortgewicht	:	1,60 kg/dm^3

Chemische Analyse
(slechts een indicatie)

SiO_2	:	98,9 %
Al_2O_3	:	0,60 %
Fe_2O_3	:	0,01 %
Ti_2O	:	0,04 %
CaO	:	0,02 %
MgO	:	0,01 %
K_2O	:	0,10 %
Na_2O	:	0,01 %
Gloeiverlies	:	0,20 %

Korrelverdeling

	>	1,0	mm	Slechts sporen
	>	0,8	mm	1%
0,63	-	0,8	mm	31%
0,315	-	0,63	mm	67%
	<	0,315	mm	1%

D50 0,57 mm
Andere korrelmaten op aanvraag

Verpakking

- Zakken van 25 kg op eenmalige pallets van 1000 kg met krimpfolie.
- Bigbags van 1500 kg op eenmalige pallets
- Losgestort

Neem contact met ons op voor meer informatie:

Worldwide
Tel: +31 (0)78 6546770
sales.eurogrit@sibelco.com
www.sibelco.eu

Sibelco Europe
PO Box 184
NL-3350 AD Papendrecht
The Netherlands
www.eurogrit.com

SIBELCO EUROPE

Sieving results: Small glass beads

The certified glass beads were produced from Sigmund Lindner GmbH in Germany. The roundness of particles are spherical, which results to a small internal friction angle of 14°. The beads are transparent and non-cohesive. The grain size should be 90% of the mass between 0.8 and 1.0mm grain diameter [1]. Therefore, sieves were chosen with openings 0.6, 0.85, 1.0, 1.168 and 1.4mm for this test run.

Sieve	Sieve diameter [mm]	Test 1 [g]	Test 2 [g]	Test 3 [g]	Average mass [g]
1	1.4	0.0	0.0	0.0	0.0
2	1.168	0.1	0.1	0.1	0.1
3	1.0	57.2	72.0	54.5	61.2
4	0.85	105.9	87.4	98.1	97.1
5	0.6	3.9	3.6	7.8	5.1
6	dustpan	0.0	0.0	0.0	0.0
	total	185.6	153.9	148.6	162.8

Table A.7: Test results with small glass beads

Sieve	Sieve diameter [mm]	Average mass [g]	Cumulative mass [g]	Passing cumulative mass percentage [%]
1	1.4	0.0	0.0	100.0
2	1.168	0.1	0.1	99.9
3	1.0	61.2	61.3	62.5
4	0.85	97.1	158.4	3.1
5	0.6	5.1	163.5	0
6	dustpan	0.0	163.5	0

Table A.8: Test results with small glass beads

The density in dry state was $2500 kg/m^3$. The internal friction angle wa 14°.

The D_{50} was 1.13mm by interpolating the sieve meshes between 1.0 and 1.168mm. The grain grading was very homogeneous. Major beads fell

[1] http://www.sigmund-lindner.com/

into two sieves, which can be considered as unreliable. This method was insufficient to get an accurate grain size distribution. In addition, the particles size was not aligned with the manufacture sheet. The roundness was spherical due to the artificial production process, which characterised the homogeneous package of this material. As a result, a relative steep grain size distribution appeared with only three valid points in semi-loggraph. Additional analysis for beads was not possible with this sieving method.

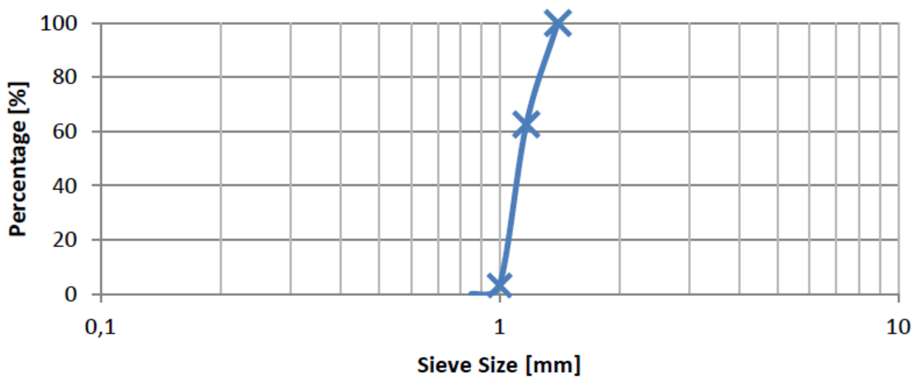

Figure A.4: Particle Size Distribution: small beads

For more accurate beads diameter method of laser diffraction analysis or imaging particle analysis.

Sieving results: Large glass beads

The certified glass beads were produced from Sigmund Lindner GmbH in Germany. The roundness of particles are spherical, which results in a small internal friction angle of 13°. The beads are transparent and non-cohesive. The grain size should be 90% of the mass between 1.25 and 1.65mm grain diameter [2]. Sieves with meshes 1.0, 1.168, 1.4, 1.65 and 1.8mm were used for this test runs.

The density in dry state is $2500kg/m^3$. The internal friction angle is 13°.

[2] http://www.sigmund-lindner.com/

Sieve	Sieve diameter [mm]	Test 1 [g]	Test 2 [g]	Test 3 [g]	Average mass [g]
1	1.8	0.0	0.0	0.0	0.0
2	1.65	4.3	3.2	4.9	4.1
3	1.4	104.7	92.4	101.9	99.7
4	1.168	76.3	58.0	41.4	58.7
5	1.0	0.3	0.3	0.3	0.3
6	dustpan	0.0	0.1	0.1	0.0
	total	167.1	163.1	160.5	163.5

Table A.9: Test results with large glass beads

Sieve	Sieve diameter [mm]	Average mass [g]	Cumulative mass [g]	Passing cumulative mass percentage [%]
1	1.8	0.0	0.0	100.0
2	1.65	4.1	4.1	97.5
3	1.4	99.7	103.8	36.2
4	1.168	58.7	162.5	0.2
5	1.0	0.3	162.8	0.0
6	dustpan	0.0	162.8	0.0

Table A.10: Test results with large glass beads

The grain size was between 1.25 and 1.65mm according to the prescript. The D_{50} was 1.45mm by interpolating sieve openings between 1.4 and 1.65mm. Major beads fell into two sieves, which causes to unreliable results. The particles sieve analysis was insufficient to get an accurate grain size distribution graph, although the D_{50} was within the given limits. The roundness is spherical due to the artificial production process. Also, a high percentage of the beads fell only in two sieves, which proved for the homogeneous package of this material. A narrow gradation appeared with the data points in the semi-loggraph, which made it an inaccurate outcome for a grain size distribution analysis.

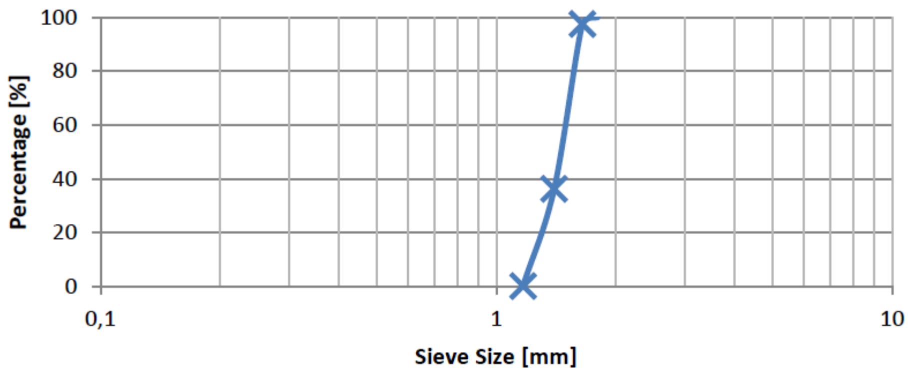

Figure A.5: Particle Size Distribution: small beads

Conclusion

The following D_{50} are shown in Table A.11 for sand and glass beads. Calculation were made with the values from the particle sieve analysis or the production sheets.

Type sand	Diameter $[mm]$	Internal friction angle	Uniformity coefficient
Dorsilit 5F	1.41	33	1.42
Dorsilit 7	0.93	33	1.34
Dorsilit 8	0.63	32	1.52
Large glass beads	1.45	13	xx
Small glass beads	1.13	14	xx

Table A.11: Sieve result of sand

The sand packages were classified as sub round with internal friction angle of around 32°. Gradation was very poorly graded, since the uniformity coefficient was close to one. Glass beads were even worse graded with an unknown uniformity coefficient. The beads fell only in two sieves by the homogeneous particle size. The internal friction angles were respectively 14° and 13° for small and large glass beads.

Appendix B

Water system design

This appendix described the design process with a starting point and considerations to get the final jet system. An acrylic flume is assigned to the experiments with a vertical submerged hydraulic plain jet. Many aspects were considered to get the final experiment set-up. The experiments were executed at the Dredging laboratory at faculty 3ME at Delft. The plain jet was produced by Demon in Delft.

Starting point

The main objective was to see the 2D effect beneath the hydraulic plain jet. The starting point was the plain jet with a width of $2.5mm$ nozzle diameter, which is a reasonable dimension for the test flume. Also, one goal was to try to duplicate the experiment from Rajaratnam [1981] with the same jet width. The form of jet was free to accommodate the research preferences.

Considerations for jet

The 3D effects should be excluded in the test system(normal-direction). The normal length must be at least twenty times the width of the nozzle Koched et al. [2011]. The nozzle width was $2.5mm$. The length should be at least $20 * 2.5 = 50mm$. The length was doubled to create some space for preparations in the soil before each run. The nozzle was, therefore, designed with an inner length of $100mm$.

The thickness of the hull was determined at $2mm$ for all the walls of the draghead. The jet and the tube were made from aluminium. The jet barely bend as calculated with the forget-me-not formulas. The assumption was made with the outflow of $2.5m/s$, which was converted to the pressure via equation 2.1. The bending in the draghead was calculated to $8.7 * 10^{-4}m$, which was neglectable and did not caused any problem during the tests.

$$w = \frac{5}{384}\frac{q * l^4}{EI} = \frac{5}{384}\frac{(\frac{1000*2.5^2}{2}) * 0.1^4}{70 * 10^9 * \frac{0.1*0.002^3}{12}} = 8.7 * 10^{-4}m \tag{B.1}$$

Other consideration was to clamp the jet to the frame.

$$w = \frac{1 * F * l^3}{3 * EI} \tag{B.2}$$

$$w = \frac{1 * (\frac{1000*2.5^2}{2}) * 1.3^3}{\frac{3*70*((0.104*0.054^3)-(0.104-2*0.002)(0.104-2*0.002)^3}{12}} = 0.4 * 10^{-4}m \tag{B.3}$$

The inner dimension of the nozzle width is $50mm$. The vertical velocity in the draghead must be much larger than the vertical outflow from the nozzle. $u_0 >> w_0$ with in mind the volume balance $Q_d = Q_n$. $b_0 * l * u_0 = b_1 * l * w_0$ The broader draghead created an hydraulic drop at the opening with acceleration in the funnel, which was curved as two quarter circle with a radius of $25mm$. This shape provided the most uniform outflow with less turbulence than other nozzle shapes.

The draghead had a rectangular shape with a length of $300mm$ in longitudinal direction. Suspended particles could accumulation on top of the head during test. A longer head should avoid any deposition of grains on the jet, but more length separates hydraulic interaction on both sides of the jet. Compromise was made on top of the draghead one meter long round aluminium pipe, where the fluid can flow around and the jet arm had sufficient length to clamp for several SOD.

The final dimensions of plain jet and frame could be found on page B5.

Considerations for flume

The overall outer dimensions of the flume is 1.5*0.75*1.0m (lxbxh), which was manufactured from transparent acrylic. The walls, bottom, weirs and ridges have a wall thickness of $10mm$. The flume had initially two compartments with a $0.9m$ height weir in the middle of the normal length. The water level was set to $0.9m$ during the experiments. Any waves would damp out by the overflow of the high weir.

The water jet had to fit the concerning cell. The hydraulic jet was made from a $2mm$ thick plate by cutting, bending and welding. This results in an outer dimension of jet $100 + 2 * 2 = 104mm$. The added weir had $110mm$ space behind the inner front wall. The larger length was chosen for avoiding any jams between the jet and the added acrylic walls.

The flume is divided in three compartments with respectively 0.7 and $0.9m$ height transparent weirs between the front, middle and back cells. The $0.7mm$ height weir is a bit lower, but still the holds the majority of the suspended particles inside the front compartment in the high values of the erosion parameter. The higher $0.9mm$ weir holds smaller particles from the back compartment.

The limitation to this research is the width of the flume with $0.75mm$. An experiments should avoid any particle depositions against the side wall. This could affect the outcomes of the dimensions of the eroded cavity. Therefore, assumptions was made that the soil bed remain at original bed level for about one-third of the flume width.

Other considerations

The experiments are executed in the front compartment with the hanging plain jet on a stiff frame. The frame has a clamp system for the jet, so the stand off distances can be adjusted to the required impinging distance between the nozzle and the sand bed.

As mentioned, the cavity width has a maximum of $0.5m$ to avoid any deposition against the side walls. The sand hole has a ratio of 0.25 in relation to depth-width (Rajaratnam [1981]). The cavity depth would be at the maximum of $0.125m$. The sand bed is prepared to $0.2m$ level for all experiments.

The discharge meter was of the brand Flowtec Variomag from type Discomaq DMT 6530, which is placed between the Y-splitter and the jet. This meter is an electromagnetic flow meter. Two pipes are mounted before and after the discharge meter for an uniform flow for an accurate measurements. The lengths of both tubes are ten times the diameter of the hose.[1] The meter has a range from 0 to $4.0m^3/h$ with an accuracy of $0.03m^3/h$

[1] https://www.erniegraves.com/egc-news/minimum-straight-pipeline-lengths-for-10-popular-flowmeters

A constant submerged pump is used for several experiments with a range of discharges. An Y-splitter was placed to direct a certain discharge to the jet, the rest recirculated back in the overflow compartment. The valves need to set up, if other outflow velocity is required. The submerged pump needs at least a discharge of $0.000625 m^3/s$. The design outflow was calculated for erosion parameter five with the largest grain size.

$$E_c = \frac{u_0}{\sqrt{H/d} * \sqrt{g\Delta D_{50}}} \tag{B.4}$$

Rewriting results in:

$$u_0 = E_c * \sqrt{H/d} * \sqrt{g\Delta D_{50}} = 5 * \sqrt{10} * \sqrt{9.81 * 1.65 * 0.00141} = 2.36 m/s \tag{B.5}$$

The value has been rounded up to $u_o = 2.5 m/s$ for a conservative approach. The minimum discharge is calculated to $Q = u * A = 2.5 * 0.0025 * 0.1 = 6.25 * 10^{-4} m^3/s$. Head losses require at least $1.25m$ head with discharges around $6.4 * 10^{-4} m^3/s$. An Ebara water pump fulfils those test requirements. The production sheet shows a maximum discharge of $240 l/min = 0.250 m^3/min = 4.2 * 10^3 m^3/s$ at $H = 2m$.

The pump is not adjustable in revolutions. The discharges can be adjusted to the experiment specifications by the two valves. One valve has been placed above the jet to lower the discharge, the second valve is mounted at the recirculation hose to increase the jet momentum for taking out the air each morning.

Two cameras were used in the experiments, namely an actioncam and a high speed camera. The actioncam was a GoPro Hero3+silver. The camera can reach a maximum of 50 frames per second with quality of 1028*960i. Videos of ten minutes were made with this device. The purpose of this camera was to capture the dimensions of cavities at the dynamic stable state at $0.5m$ in front of the flume. The second camera was a Fastcam APX Photron(grey color). The camera has an 8Gb RAM memory with frame quality of 1024*1024 and 1500 frames per second. The actual width is $140mm$, so each millimeter is about 7.3pixels ($1024/140 = 7.31 pixel/mm$). The film rate per second is set to 1500 for all tests, so that the smallest particles in high velocity outflow do not blur in a frame. This camera is mainly used in purpose for the start phase, since the record timespan is just 6.67 seconds.

A table for the pressure gauges were used to test the potential flow in the normal direction at an impinging level. The static head should not differ

$D_50[mm]$	Pixel per grain[-]
0.63	4.6
0.93	6.8
1.41	10.3

in case of a plain jet. The pressure gauge is placed at $15mm$ and $50mm$ behind the front wall.

Test

The experiments are as followed prepared in the flume. Fresh water is filled in the three compartments to a water level of $0.9m$. All test attributes are coupled and set-up for the experiments. This setting rests for 24hours to adapt the environmental temperature. The pump is started for pushing out air in the water system every morning. After some time, preparations are made for a flat soil bed.

Before the main experiment, the jet has to be tested for any outflow in the normal directions. The set-up is made to prove the plain jet with the pressure gauges in plastic flat table. The pressure opening is at the soil bed height of $0.2m$ at $15mm$ or $50mm$ from the front panel. Another test is a pressure gauge in free flow, which is secured to a fixed standing pole.

After each test run, the bed has to be prepared for the next test. The soil was flattened to an homogeneous bed state with a peddle. The jet stand off distance or discharge are adjusted to the test requirements. The cameras started before the pump is turned on.

If dens bed is tested, a long vibrator is used to dense the soil bed by adding extra weighted grains to the specified soil volume. The vibrator can only be turned on/off to one amplitude and frequency. An homogeneous bed is assumed in the soil in length, width and depth after preparations. The aim is whether the erosion parameter is related to density of soil.

Bentonite is mixed in dry state of 3.6% of a sand mass. Mixture is put in the front compartment without water. Flume is slowly filled with water to $900mm$ height and let it rest for 24 hours.

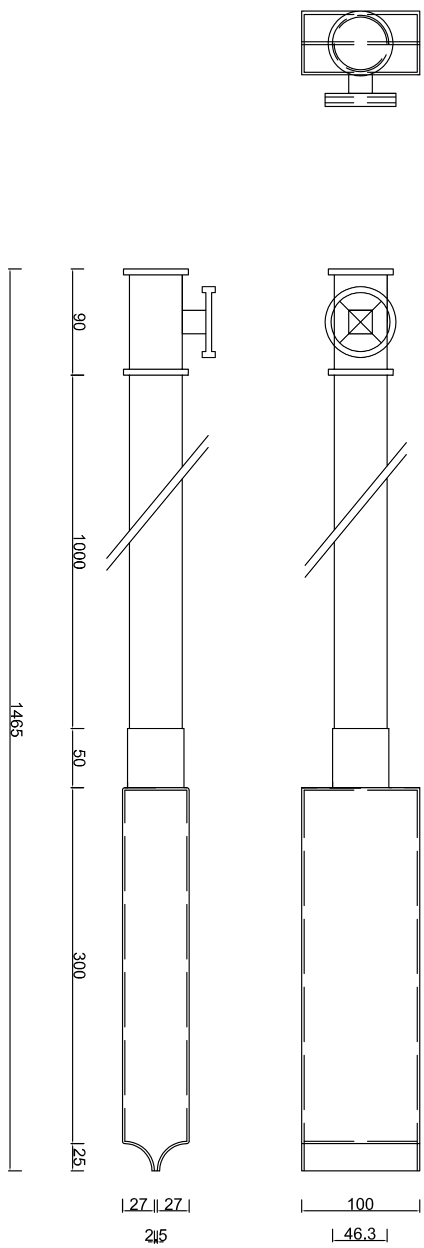

Name: Chi-Fung Wu	Plain jet	Unit: mm
Date: 10 January 2017		

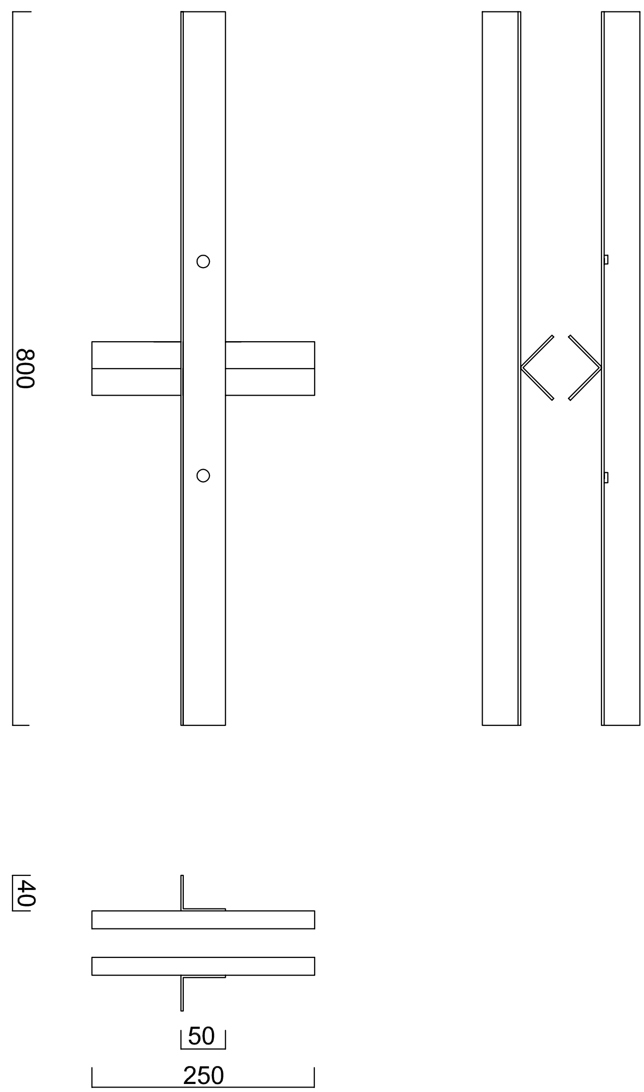

Name: Chi-Fung Wu	Frame	Unit: mm
Date: 10 January 2017		

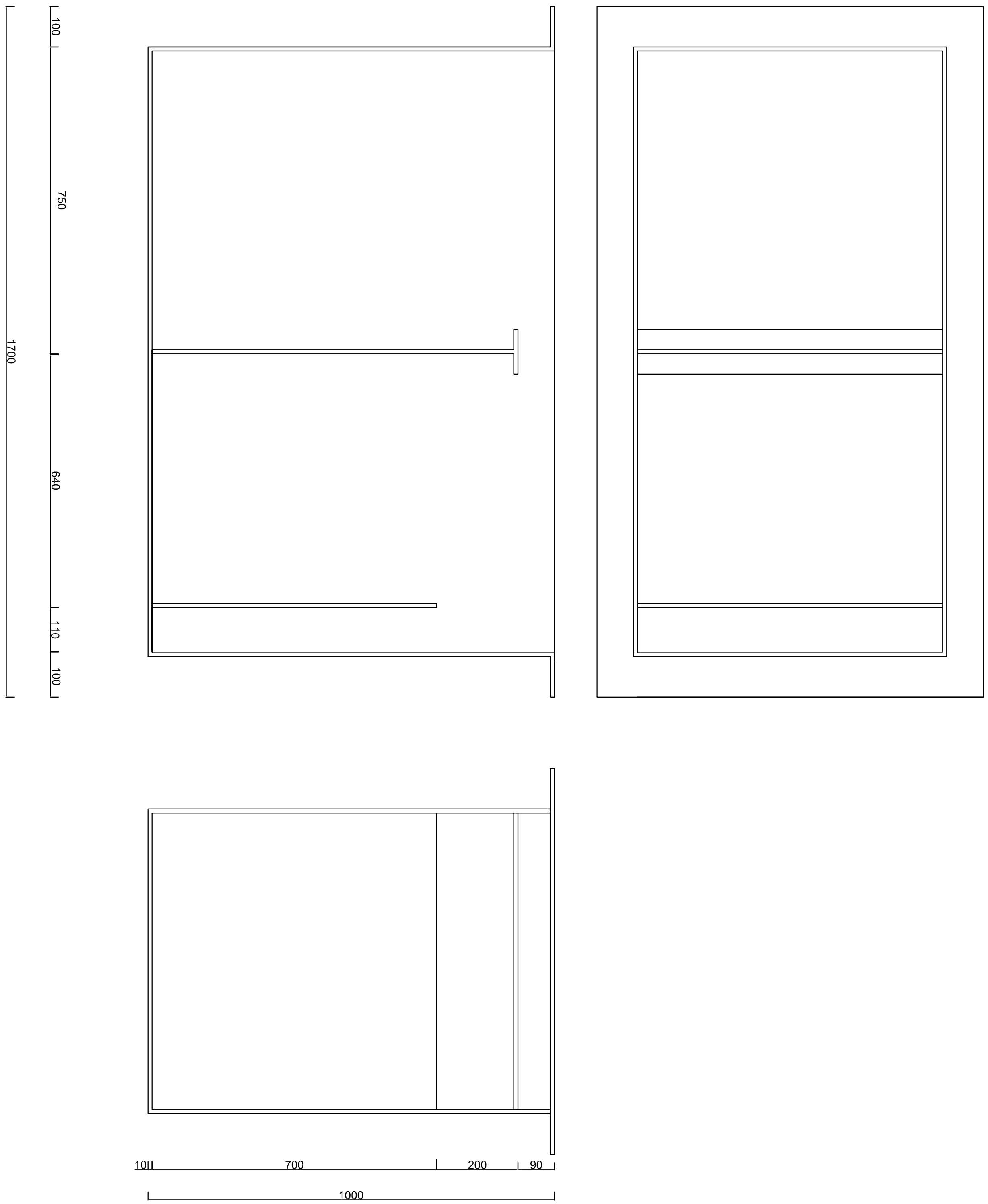

Name: Chi-Fung Wu

Date: 10 January 2017

Flume

Unit: mm

Water jet

The aims of frame and water jet were to get quantitative measuring results and its distribution in several conditions.

So test set-up can vary in:

- Outflow velocity
- Stand of distance
- Grain size
- Density

These parameters results in:

- Cavity depth
- Cavity width
- Cavity hill height
- Cavity development in time

Appendix C

Validation system

This research deals with a plane jet. An important subject is that the jet behaves only in 2-dimensional (longitudinal and lateral) directions. The normal effect has to be avoided to get representable results. Any 3-dimensional are tested with the impermeable impinging and free jet.

Impinging jet

Two pressure gauges has been placed at $15mm$ and $50mm$ beneath the nozzle in normal direction in impinging and free jet-setting with the plane jet. Vertical pressure is measured thirty seconds for getting averaged and bandwidth value at stationary phase. This test was done with $D_{50} = 0.63mm$ in SOD=10. These values are converted to stagnation pressure in Table C.2.

The vertical middle gauge values are slightly higher for several fluid outflow in impinging jet than the front gauge. Normal effect can be neglect for this impinging jet. Percentage differences are around 3% of the measured values between front and middle gauges. Two exception of 13% and 9% were at the outflow velocity of $0.4m/s$ and $0.8m/s$, but in absolute values are neglectable difference. Very small leakage between the impinging and the front wall lowers the pressure. This means a small net force is present from center in normal directions. Also the wall friction could have a minor effect to the results of the front gauges. Assumption could be made that bearly any water slipped through the joint between the surface and the front wall.

Velocity $[m/s]$	Front gauge $[kPa]$	Middle gauge $[kPa]$	Front stagnation head $[mm]$	Middle stagnation head $[mm]$	Difference [%]
0.3	0.06	0.06	6	6	0
0.4	0.08	0.09	8	9	13
0.8	0.31	0.34	32	35	9.7
1.2	0.62	0.64	63	65	3.2
1.6	1.17	1.21	119	123	3.4
2.0	2.12	2.16	216	220	1.9
2.4	2.58	2.65	263	270	2.7

Table C.1: Stagnation head beneath plain jet $z = 15mm$ and $z = 50mm$

Small fluctuation are expected from a turbulent impinging jet. Measured values are presented in the Table below:

Velocity $[m/s]$	Front gauge $[kPa]$	Middle gauge $[kPa]$	Front fluctuation $[kPa]$	Middle fluctuation $[kPa]$	Percentage [%]	Percentage [%]
0.3	0.06	0.06	0.02	0.02	33	33
0.4	0.08	0.09	0.03	0.02	38	22
0.8	0.31	0.34	0.07	0.08	23	24
1.2	0.62	0.64	0.10	0.09	16	14
1.6	1.17	1.21	0.17	0.22	15	18
2.0	2.12	2.16	0.27	0.34	13	16
2.4	2.58	2.65	0.29	0.43	11	16

Table C.2: Stagnation head in normal directions

Turbulence is around 20% of the mean vertical stagnation pressure. The presents of fluctuation shows a small instability of impinging jet during the test. Vortices occurs on both side from the centerline with a swaying stagnation point. The turbulence indicates some flow processes in the lateral directions.

Tables C.3 and C.4 represent the results of pressure head of impinging and free jet at different SOD.

H/d	Outflow velocity [m/s]	Average static head[m]	Fluctuation[m]
10	0.4	0.09	0.02
10	1.2	0.64	0.09
10	2.0	2.16	0.34
20	0.4	0.03	0.02
20	1.2	0.40	0.09
20	2.0	1.22	0.31
30	0.4	0.03	0.02
30	1.2	0.25	0.07
30	2.0	0.77	0.12

Table C.3: Vertical velocity in impinging jet

H/d	Outflow velocity	Average static head	Fluctuation
10	0.4	0.10	0.03
10	1.2	0.77	0.1
10	2.0	2.14	0.26
20	0.4	0.04	0.01
20	1.2	0.38	0.07
20	2.0	1.15	0.19
30	0.4	0.07	0.02
30	1.2	0.31	0.07
30	2.0	0.75	0.11

Table C.4: Vertical velocity in free jet

The flow characteristics of plain impinging jet are considered here in the lateral directions at $SOD = 10$. The Table C.5, C.6, C.7 and C.8 are the measured vertical pressure for test at $SOD = 10$. Figure C.1 gives the overview of those tables. A normalised Gaussian distributed is the pressure distribution beneath the jet.

Free jet

Two pressure gauges are mounted at a firm screw-threads at the bottom of the flume. These are placed at the same location as the impinging jet from the previous tests. The gauges have measured the pressure for 30 seconds at stationary phase as stated in Table below. The tests were executed at

Velocity $[m/s]$	Theoretical pressure $[kPa]$	Theoretical head $[mm]$	Stagnation pressure $[kPa]$	Stagnation head $[mm]$	Normalised stagnation head $[-]$
0.3	0.046	4.6	0.02	2.0	0.444
0.4	0.086	8.2	0.03	3.1	0.375
0.8	0.326	32.6	0.18	18.3	0.563
1.2	0.734	73.4	0.40	40.8	0.555
1.6	1.305	130.5	0.68	69.3	0.531
2.0	2.248	224.8	1.22	124.4	0.553
2.4	2.936	293.6	1.38	140.7	0.479

Table C.5: Stagnation head at plain jet $x = 0mm$

Velocity $[m/s]$	Theoretical pressure $[kPa]$	Theoretical head $[mm]$	Stagnation pressure $[kPa]$	Stagnation head $[mm]$	Normalised stagnation head $[-]$
0.3	0.046	4.6	0.01	1.0	0.222
0.4	0.086	8.2	0.03	3.1	0.375
0.8	0.326	32.6	0.13	13.3	0.406
1.2	0.734	73.4	0.28	28.5	0.389
1.6	1.305	130.5	0.49	49.9	0.383
2.0	2.248	224.8	0.91	92.8	0.413
2.4	2.936	293.6	0.99	100.9	0.344

Table C.6: Stagnation head at plain jet $x = 5mm$

$SOD = 10$ for several outflow velocities.

The deviations are all smaller than 5% of the vertical averaged pressure. Between the front and the middle gauges are slightly different, which means the occurrence of normal flow beneath the free jet. The instant measurements show that the water stream varies at all time for all jet momentum with 15% of the averaged pressure, but smaller velocities has relatively large deviation.

Velocity $[m/s]$	Theoretical pressure $[kPa]$	Theoretical head $[mm]$	Stagnation pressure $[kPa]$	Stagnation head $[mm]$	Normalised stagnation head $[-]$
0.3	0.046	4.6	0.01	1.0	0.222
0.4	0.086	8.2	0.02	2.0	0.250
0.8	0.326	32.6	0.06	6.1	0.188
1.2	0.734	73.4	0.12	12.2	0.167
1.6	1.305	130.5	0.21	21.4	0.164
2.0	2.248	224.8	0.36	36.7	0.163
2.4	2.936	293.6	0.40	40.8	0.139

Table C.7: Stagnation head at plain jet $x = 10mm$

Velocity $[m/s]$	Theoretical pressure $[kPa]$	Theoretical head $[mm]$	Stagnation pressure $[kPa]$	Stagnation head $[mm]$	Normalised stagnation head $[-]$
0.3	0.046	4.6	0.00	0.0	0.000
0.4	0.086	8.2	0.00	0.0	0.000
0.8	0.326	32.6	0.04	4.1	0.125
1.2	0.734	73.4	0.05	5.1	0.069
1.6	1.305	130.5	0.07	7.1	0.055
2.0	2.248	224.8	0.09	9.2	0.041
2.4	2.936	293.6	0.10	10.2	0.035

Table C.8: Stagnation head at plain jet $x = 20mm$

Velocity $[m/s]$	Front gauge $[kPa]$	Middle gauge $[kPa]$	Front fluctuation $[kPa]$	Middle fluctuation $[kPa]$	Percentage Front-middle [%]	Percentage fluctuation [%]
0.3	0.08	0.02	0.08	0.02	25	25
0.4	0.10	0.03	0.10	0.03	30	30
0.8	0.33	0.04	0.34	0.05	12	15
1.2	0.76	0.10	0.77	0.10	13	13
1.6	1.16	0.18	1.13	0.19	16	17
2.0	2.10	0.24	2.14	0.26	11	12
2.4	2.51	0.43	2.56	0.48	17	19

Table C.9: Stagnation pressure in normal directions for free jet

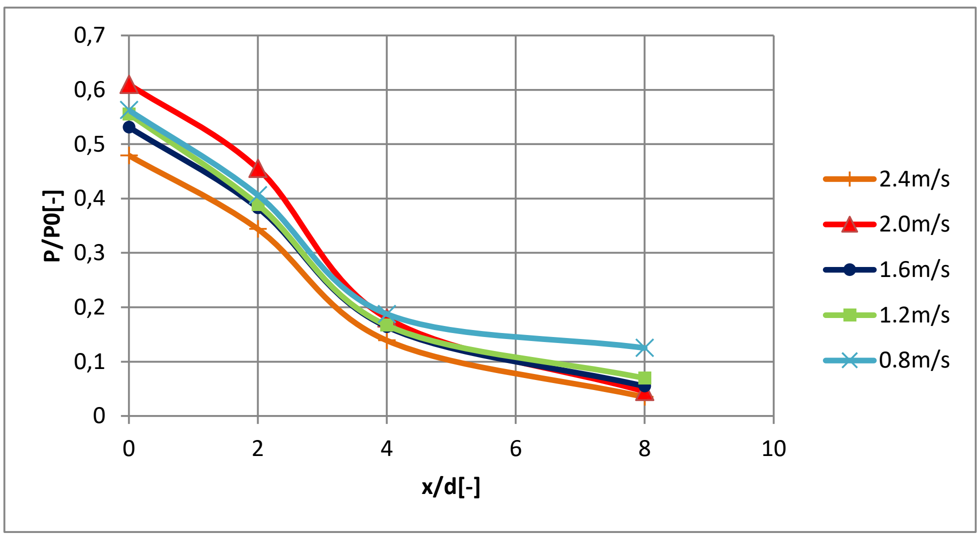

Figure C.1: Normalised pressure distribution

Appendix D

Test Results

All the results of the experiment for this research can be found here. The experiment has been done carefully to produce accurate outcome. The tables shows an extensive data, which has been produced during the test period. Only the good representative results has been added to table for a good solid conclusion. Test failures, like wrong setting of outflow velocity, is filtered out after thoughtful thinking. Please note that some test has a higher density of bed or has a mixture with bentonite.

Experimental results

First specific test $D_{50} = 0.63mm$, $u_0 = 2m/s$ and $SOD = 10$ are tested thrice for an accuracy test.

Dynamic bed state occurs at many test, which varies the maximum depth continuous in time. The deepest cavity depth has been visually measured after 20 minutes.

Time [s]	Test 1 [mm]	Test 2[mm]	Test 3[mm]
0	0	0	0
0.05	5	4	5
0.10	12	10	10
0.15	17	18	18
0.20	26	27	24
0.25	31	34	30
0.30	35	41	37
0.35	42	45	39
0.40	44	46	42
0.45	41	51	43
0.50	43	52	45
0.55	46	54	47
0.60	53	55	50
0.65	54	57	48
0.70	55	57	51
0.75	55	58	53
0.80	58	58	53
0.85	59	59	54
0.90	59	60	56
0.95	58	61	58
1.0	59	62	58

Table D.1: Observations for accuracy

Test	H/d [−]	Grain size[mm]	Specific gravity [−]	Nozzle velocity [m/s]	Erosion parameter [−]	Hill height [mm]	Cavity depth [mm]	Cavity width [mm]	Reynolds number [−]
1	30	0.63	1.6	2.00	3.62	31	78	159	5000
2	10	0.63	1.6	1.20	3.75	30	49	136	3000
3	10	0.63	1.6	2.00	6.26	43	82	179	5000
4	10	0.93	1.6	2.00	5.15	27	78	129	5000
5	10	0.63	1.6	2.00	6.26	37	81	167	5000
6	10	1.45	1.6	2.00	4.12	10	65	118	dens
7	10	1.41	1.6	2.00	4.20	19	61	95	5000
8	10	1.41	1.6	2.00	4.20	17	57	92	5000
9	30	1.41	1.6	0.95	1.16	25	34	87	2350
10	30	1.41	1.6	0.55	0.69	11	12	49	1400
11	30	1.41	1.6	0.35	0.43	0	0	0	875
12	30	1.41	1.6	0.70	0.89	15	18	64	1800
13	30	1.41	1.6	0.75	0.92	21	13	63	1875
14	30	1.41	1.6	2.10	2.61	30	55	116	5300
15	30	1.41	1.6	0.45	0.54	6	9	39	1100
16	30	1.41	1.6	0.40	0.52	5	4	34	1050
17	30	1.41	1.6	4.90	6.04	48	143	230	12250
18	30	1.41	1.6	2.40	3.01	28	63	129	6000
19	30	1.41	1.6	5.05	6.22	57	153	241	12625
20	30	1.41	1.6	5.10	6.26	58	155	249	12700
21	30	1.41	1.6	3.60	4.41	39	98	178	8950
22	30	1.41	1.6	3.00	3.72	33	88	156	7550
23	30	1.41	1.6	2.40	2.93	28	64	130	5950
24	30	1.41	1.6	2.00	2.4	27	48	105	5000
25	30	1.41	1.6	0.75	0.90	17	19	63	1825

Table D.2: Test 1-25 results

Test	H/d [−]	Grain size[mm]	Specific gravity [−]	Nozzle velocity [m/s]	Erosion parameter [−]	Hill height [mm]	Cavity depth [mm]	Cavity width [mm]	Reynolds number [−]
26	30	1.41	1.6	1.20	1.5	19	32	78	3000
27	30	1.41	1.6	0.25	0.31	0	0	0	625
28	30	1.41	1.6	0.40	0.5	3	1	24	1000
29	30	1.41	1.6	0.80	0.99	16	17	68	2000
30	20	1.41	1.6	2.00	3.0	33	54	112	5000
31	20	1.41	1.2	3.20	4.83	36	104	153	8000
32	20	1.41	1.6	3.70	5.58	36	114	171	9250
33	20	1.41	1.6	4.50	6.79	53	158	231	11250
34	20	1.41	1.6	2.60	3.92	30	73	124	6500
35	20	1.41	1.6	1.20	1.8	25	34	77	3000
36	20	1.41	1.6	0.60	0.91	11	10	43	1500
37	20	1.41	1.6	0.40	0.6	3	4	23	1000
38	20	1.41	1.6	0.30	0.42	0	0	0	700
39	10	1.41	1.6	2.00	4.20	19	57	92	5000
40	10	1.41	1.6	1.20	2.5	9	37	53	3000
41	10	1.41	1.6	0.85	1.66	3	26	42	2125
42	10	1.41	1.6	0.30	0.58	1	2	20	750
43	10	1.41	1.6	1.90	3.66	16	63	82	4700
44	10	1.41	1.6	2.70	5.22	22	85	106	6700
45	10	1.41	1.6	3.30	6.45	30	99	143	8250
46	10	1.41	1.6	4.00	7.83	39	124	184	10050
47	10	1.41	1.6	4.65	9.06	48	153	222	11625
48	10	1.41	1.6	4.80	9.35	56	167	246	12000
49	30	0.93	1.6	2.0	3.0	42	74	176	5000
50	30	0.93	1.6	1.85	2.75	38	61	149	4625

Table D.3: Test 26-50 results

Test	H/d [−]	Grain size[mm]	Specific gravity [−]	Nozzle velocity [m/s]	Erosion parameter [−]	Hill height [mm]	Cavity depth [mm]	Cavity width [mm]	Reynolds number [−]
51	30	0.93	1.6	1.2	9.8	24	38	93	3000
52	30	0.93	1.6	1.00	1.46	23	33	96	2450
53	30	0.93	1.6	0.70	1.46	24	29	84	1750
54	30	0.93	1.6	0.40	0.6	6	12	52	1000
55	30	0.93	1.6	0.30	0.37	4	15	55	625
56	30	0.93	1.2	0.15	0.22	3	13	54	375
57	30	0.93	1.6	0.10	0.12	0	0	0	200
58	30	0.93	1.6	2.80	4.16	46	92	189	7000
59	30	0.93	1.6	3.25	4.82	47	107	203	8100
60	30	0.93	1.6	3.70	5.50	49	116	218	9250
61	30	0.93	1.6	4.30	6.39	57	142	247	10750
62	30	0.93	1.6	3.90	5.80	51	126	224	9750
63	20	0.93	1.6	3.90	7.22	46	129	212	9750
64	20	0.93	1.6	4.20	7.77	54	145	236	10500
65	20	0.93	1.6	3.40	6.29	39	108	184	8500
66	20	0.93	1.6	2.0	3.6	30	68	133	5000
67	20	0.93	1.6	1.70	3.15	25	54	112	4250
68	20	0.93	1.6	1.2	2.2	18	39	86	3000
69	20	0.93	1.6	0.85	1.57	15	27	64	2125
70	20	0.93	1.6	0.40	0.7	10	14	44	1000
71	20	0.93	1.6	0.25	0.46	2	2	25	625
72	20	0.93	1.6	0.10	0.19	0	0	0	250
73	10	0.93	1.6	2.0	5.15	27	78	129	5000
74	10	0.93	1.6	1.60	4.19	21	51	87	4000
75	10	0.93	1.6	1.2	3.1	12	38	66	3000

Table D.4: Test 51-75 results

Test	H/d [−]	Grain size[mm]	Specific gravity [−]	Nozzle velocity [m/s]	Erosion parameter [−]	Hill height [mm]	Cavity depth [mm]	Cavity width [mm]	Reynolds number [−]
76	10	0.93	1.6	0.80	2.09	8	25	45	2000
77	10	0.93	1.6	0.50	1.31	4	18	34	1250
78	10	0.93	1.6	0.40	1.0	3	10	24	750
79	10	0.93	1.6	0.10	0.26	2	2	14	250
80	10	0.93	1.6	0.05	0.13	0	0	0	125
81	10	0.93	1.6	2.90	7.59	30	94	148	7250
82	10	0.93	1.6	3.25	8.51	34	108	172	8125
83	10	0.93	1.6	3.70	9.68	42	123	199	9250
84	10	0.93	1.6	4.10	10.73	48	143	238	10250
85	30	0.63	1.6	2.0	3.62	31	78	159	5000
86	30	0.63	1.6	1.60	2.94	34	64	154	4000
87	30	0.63	1.6	1.2	2.2	19	45	88	3000
88	30	0.63	1.6	0.80	1.47	25	39	119	2000
89	30	0.63	1.6	0.4	0.7	17	16	37	1000
90	30	0.63	1.6	0.30	0.55	2	13	55	750
91	30	0.63	1.6	0.20	0.37	0	0	0	500
92	30	0.63	1.6	0.25	0.46	0	0	0	625
93	20	0.63	1.6	2.0	4.4	39	79	162	5000
94	20	0.63	1.6	1.60	3.60	34	56	133	4000
95	20	0.63	1.6	1.2	2.7	30	40	114	3000
96	20	0.63	1.6	0.80	1.80	18	32	84	2000
97	20	0.63	1.6	0.50	1.12	18	28	80	1250
98	20	0.63	1.6	0.40	0.9	8	16	61	1000
99	20	0.63	1.6	0.15	0.34	0	0	0	375
100	20	0.63	1.6	2.40	5.40	43	85	182	6000

Table D.5: Test 76-100 results

Test	H/d [−]	Grain size[mm]	Specific gravity [−]	Nozzle velocity [m/s]	Erosion parameter [−]	Hill height [mm]	Cavity depth [mm]	Cavity width [mm]	Reynolds number [−]
101	20	0.63	1.6	2.80	6.80	49	106	212	7000
102	10	0.63	1.6	2.0	6.26	43	82	179	5000
103	10	0.63	1.6	1.60	5.09	20	63	118	4000
104	10	0.63	1.6	1.2	3.75	30	49	136	3000
105	10	0.63	1.6	0.80	2.54	13	29	66	2000
106	10	0.63	1.6	0.40	1.3	17	19	67	1250
107	10	0.63	1.6	0.30	0.95	10	6	28	750
108	10	0.63	1.6	0.15	0.48	0	0	0	375
109	10	0.63	1.6	2.40	7.63	39	96	175	6000
110	10	0.63	1.6	2.80	8.90	40	110	197	7000
111	10	0.63	1.6	2.00	6.26	37	85	159	5250
112	20	0.63	1.6	2.00	4.72	41	76	163	5250
113	30	0.63	1.6	2.00	3.86	50	74	193	5250
114	10	0.63	1.6	2.00	6.26	39	81	167	5250
115	10	0.63	1.6	0.30	0.95	11	4	25	750
116	10	0.63	1.6	2.40	7.63	41	96	183	6000
117	30	0.63	1.6	2.40	4.41	55	82	223	6000
118	30	0.63	1.6	2.00	3.86	50	68	183	5250
119	30	0.63	1.6	0.30	0.55	13	2	39	750
120	20	0.63	1.6	2.00	4.72	41	74	162	5250
121	30	1.13	1.6	2.00	2.88	23	53	167	5250
122	20	1.13	1.6	1.60	2.19	18	38	132	4000
123	20	1.13	1.6	1.20	1.64	16	26	110	3000
124	20	1.13	1.6	0.80	1.10	13	15	89	2000
125	20	1.13	1.6	0.25	0.34	1	1	52	625

Table D.6: Test 101-125 results

Test	H/d $[-]$	Grain size$[mm]$	Specific gravity $[-]$	Nozzle velocity $[m/s]$	Erosion parameter $[-]$	Hill height $[mm]$	Cavity depth $[mm]$	Cavity width $[mm]$	Reynolds number $[-]$
126	20	1.13	1.6	2.00	3.52	19	62	146	5250
127	20	1.13	1.6	1.60	2.68	14	44	108	4000
128	20	1.13	1.6	1.20	2.01	11	28	88	3000
129	20	1.13	1.6	0.80	1.34	7	19	64	2000
130	20	1.13	1.6	0.30	0.50	3	3	27	750
131	10	1.13	1.6	2.00	4.98	24	58	134	5250
132	10	1.13	1.6	2.00	4.98	19	63	123	5250
133	10	1.13	1.6	1.60	3.79	14	43	86	4000
134	10	1.13	1.6	1.20	2.85	9	31	65	3000
135	10	1.13	1.6	0.80	1.90	6	16	38	2000
136	10	1.13	1.6	0.25	0.59	3	4	18	625
137	10	1.13	1.6	0.40	0.95	5	7	23	1000
138	10	1.13	1.6	2.40	5.69	21	76	148	6000
139	10	1.13	1.6	2.70	6.40	26	94	179	6750
140	30	1.45	1.6	2.00	2.42	17	51	139	5000
141	30	1.45	1.6	2.00	2.54	17	52	138	5250
142	30	1.45	1.6	1.60	1.93	16	41	106	4000
143	30	1.45	1.6	1.20	1.45	11	26	84	3000
144	30	1.45	1.6	0.80	0.97	9	20	75	2000
145	20	1.45	1.6	0.40	0.48	2	4	31	1000
146	30	1.45	1.6	0.25	0.30	0	0	0	625
147	30	1.45	1.6	2.40	2.90	22	62	149	6000
148	30	1.45	1.6	2.80	3.38	26	78	165	7000
149	30	1.45	1.6	2.00	3.11	12	56	127	5250
150	30	1.45	1.6	1.60	2.37	10	43	93	4000

Table D.7: Test 126-150 results

Test	H/d $[-]$	Grain size$[mm]$	Specific gravity $[-]$	Nozzle velocity $[m/s]$	Erosion parameter $[-]$	Hill height $[mm]$	Cavity depth $[mm]$	Cavity width $[mm]$	Reynolds number $[-]$
151	20	0.63	1.6	1.20	1.77	6	31	72	3000
152	20	0.63	1.6	0.80	1.18	7	23	59	2000
153	20	0.63	1.6	0.40	0.59	3	9	32	1000
154	20	0.63	1.6	0.25	0.37	0	0	0	625
155	20	0.63	1.6	2.40	3.55	16	68	126	6000
156	20	0.63	1.6	2.80	4.14	17	80	147	7000
157	10	0.63	1.6	2.00	4.12	10	65	118	5250
158	10	0.63	1.6	1.60	3.35	5	49	73	4000
159	10	0.63	1.6	1.20	2.51	3	32	50	3000
160	10	0.63	1.6	0.80	1.67	2	22	38	2000
161	10	0.63	1.6	0.40	0.84	1	9	22	1000
162	10	0.63	1.6	0.25	0.52	1	4	12	625
163	10	0.63	1.6	2.40	5.02	15	72	122	6000
164	10	0.63	1.6	2.80	5.86	17	88	148	7000
165	10	0.63	1.6	3.20	6.69	21	97	164	8000
166	10	0.63	1.6	2.0	6.26	44	86	170	bentonite

Table D.8: Test 151-166 results